PROBING THE OUTSKIRTS OF THE EARLY-STAGE GALAXY CLUSTER MERGER A1750

Massachusetts Institute of Technology

PROBING THE OUTSKIRTS OF THE EARLY-STAGE GALAXY CLUSTER MERGER A1750

ESRA BULBUL[1], SCOTT W. RANDALL[1], MATTHEW BAYLISS[1,2], ERIC MILLER[3], FELIPE ANDRADE-SANTOS[1], RYAN JOHNSON[4],
MARK BAUTZ[3], ELIZABETH L. BLANTON[5], WILLIAM R. FORMAN[1], CHRISTINE JONES[1], RACHEL PATERNO-MAHLER[5,6],
STEPHEN S. MURRAY[1,7], CRAIG L. SARAZIN[8], RANDALL K. SMITH[1], AND CEMILE EZER[9]
[1] Harvard-Smithsonian Center for Astrophysics, 60 Garden Street, Cambridge, MA 02138, USA
[2] Department of Physics, Harvard University, 17 Oxford Street, Cambridge, MA 02138, USA
[3] Kavli Institute for Astrophysics & Space Research, Massachusetts Institute of Technology, 77 Massachusetts Avenue, Cambridge, MA 02139, USA
[4] Department of Physics, Gettysburg College, Gettysburg, PA 17325, USA
[5] Astronomy Department and Institute for Astrophysical Research, Boston University, 725 Commonwealth Avenue, Boston, MA 02215, USA
[6] Department of Astronomy, University of Michigan, 1085 S. University Avenue, Ann Arbor, MI 48109, USA
[7] Department of Physics and Astronomy, Johns Hopkins University, 3400 N. Charles Street, Baltimore, MD 21218, USA
[8] Department of Astronomy, University of Virginia, P.O. Box 400325, Charlottesville, VA 22904, USA
[9] Department of Physics, Boğaziçi University, Istanbul, Turkey

ABSTRACT

We present results from recent *Suzaku* and *Chandra* X-ray and Multiple Mirror Telescope optical observations of the strongly merging "double cluster" A1750 out to its virial radius, both along and perpendicular to a putative large-scale structure filament. Some previous studies of individual clusters have found evidence for ICM entropy profiles that flatten at large cluster radii, as compared with the self-similar prediction based on purely gravitational models of hierarchical cluster formation, and gas fractions that rise above the mean cosmic value. Weakening accretion shocks and the presence of unresolved cool gas clumps, both of which are expected to correlate with large-scale structure filaments, have been invoked to explain these results. In the outskirts of A1750, we find entropy profiles that are consistent with self-similar expectations, and gas fractions that are consistent with the mean cosmic value, both along and perpendicular to the putative large-scale filament. Thus, we find no evidence for gas clumping in the outskirts of A1750, in either direction. This may indicate that gas clumping is less common in lower temperature ($kT \approx 4$ keV), less massive systems, consistent with some (but not all) previous studies of low-mass clusters and groups. Cluster mass may, therefore, play a more important role in gas clumping than dynamical state. Finally, we find evidence for diffuse, cool (<1 keV) gas at large cluster radii (R_{200}) along the filament, which is consistent with the expected properties of the denser, hotter phase of the warm–hot intergalactic medium.

Key words: galaxies: clusters: individual (A1750) – large-scale structure of universe – X-rays: galaxies: clusters

1. INTRODUCTION

Galaxy cluster mergers are ideal probes of gravitational collapse and the hierarchical structure formation in the universe. Observations of the evolving cluster mass function provide a sensitive cosmological test that is both independent of, and complementary to, other methods (e.g., BAO, SN, CMB; Vikhlinin et al. 2009). The use of galaxy clusters as cosmological probes relies on the accuracy of scaling relations between the total mass and observable quantities. Galaxy cluster mergers will disrupt the intracluster gas and cause departures from these scaling relations (e.g., Randall et al. 2002; Wik et al. 2008). Given that these mass scaling relations are a necessary ingredient for the interpretation of ongoing cosmological surveys, a detailed understanding of the intracluster medium (ICM) gas physics in mergers has become increasingly important.

The properties of the ICM in the cores of merging clusters have been studied in detail, since the high density and surface brightness of the gas in this region is well suited to high angular resolution observations with *Chandra* and *XMM-Newton* (see Markevitch & Vikhlinin 2007, for a review). With the launch of the low particle-background *Suzaku* mission, it has become possible to probe the low gas density and faint surface brightness regions at the virial radii of nearby galaxy clusters (e.g., Bautz et al. 2009; Akamatsu et al. 2011; Miller et al. 2012; Sato et al. 2014; Urban et al. 2014). Observational studies at these radii have mostly focused on relatively relaxed,

massive, cool-core systems. Due to the limited number of observations, the dynamical evolution of the ICM in strong merger events out to the virial radius is not clearly understood. Strongly merging, bimodal clusters are where we expect to find the large-scale filaments and accretion shocks. Comparing results from observations of mergers and relaxed clusters at the virial radius will provide an important confirmation of our current picture of large-scale structure formation. The double clusters identified from *Einstein* observations (A1750, A98, A115, A3395) are ideal targets for studying the virial radii of strongly merging clusters (Forman et al. 1981). These canonical binary galaxy clusters have two separated peaks of X-ray emission, and distortions in their X-ray surface brightness distributions suggest ongoing merger events (e.g., Paterno-Mahler et al. 2014). Most of these systems are in fact triple clusters, with all subclusters lying roughly along the same line, suggesting the presence of large-scale structure filaments.

A1750 is a triple merger system at a redshift of 0.085, with an average temperature of 4.5 keV (De Grandi & Molendi 2002; Neumann 2005). It contains three main subclusters with X-ray centroids: A1750N (J2000, R.A.: 202°79, decl.: −1°73), A1750C (J2000, R.A.: 202°71, decl.: −1°86), and A1750S (J2000, R.A.: 202°54, decl.: −2°105). Multiple Mirror Telescope (MMT) data provided redshifts for the brightest cluster galaxies of 0.0836, 0.0878, and 0.0865 (see Section 5 for details). A1750 was identified as a strongly merging "double" cluster due to the presence of two bright X-ray

Table 1
Summary of the *Suzaku* and *Chandra* X-Ray Pointings

Satellite	Pointing	ObsID	R.A.	decl.	Date Obs	Exposure XIS0/XIS1/XIS3 (ks)	PI
Suzaku	North	806096010	13 31 15.53	−01 39 13.3	2011 Jul 2	74.7/74.7/74.7	S. Randall
Suzaku	Center	806095010	13 30 46.63	−01 53 14.3	2011 Jul 24	38.0/38.0/38.0	S. Randall
Suzaku	South	806097010	13 30 13.15	−02 06 22.7	2011 Jul 9	70.2/70.2/70.2	S. Randall
Suzaku	Southeast	806098010	13 31 27.19	−02 04 19.9	2011 Jul 6	55.9/55.9/56.0	S. Randall
Suzaku	Southeast	806098020	13 31 28.58	−02 02 29.4	2011 Dec 23	11.3/11.3/11.3	S. Randall
Chandra	North	11878	13 31 10.83	−01 43 21.0	2010 May 11	19.4[a]	S. Murray
Chandra	Center	11879	13 30 50.30	−01 52 28.0	2010 May 9	19.7[a]	S. Murray
Chandra	South	12914	13 30 15.80	−02 02 28.7	2011 Mar 16	36.8[a]	S. Murray

Note.
[a] ACIS-I.

subcluster peaks, which are clearly visible in the *Einstein* image (Forman et al. 1981). The centers of A1750N and A1750C are separated by $9\farcm7$ (930 kpc; see Figure 2). *ASCA* and *ROSAT* observations indicate possible shock-heated gas with an elevated temperature of 5.5 keV between these subclusters, suggesting that they are in an early-stage merger (Donnelly et al. 2001). More recent *XMM-Newton* observations confirm this region of elevated temperature, and also indicate that A1750C may itself be undergoing a merger (Belsole et al. 2004). A1750S was identified with *ROSAT* observations. Its center is located $17\farcm5$ (1.68 Mpc) to the southwest of A1750C, along the same line connecting A1750C and A1750N, presumably tracing a large-scale filament. The 0.2–10 keV luminosities of the two brighter subclusters are 1.3×10^{44} erg s^{-1} for A1750N and 2.2×10^{44} erg s^{-1} for A1750C (Belsole et al. 2004). The X-ray luminosity of the fainter, southern subcluster A1750S is 6.4×10^{43} erg s^{-1}, estimated from *ROSAT* PSPC observations.

Here, we present results from mosaic *Suzaku* observations of A1750 out to the virial radius. These new observations, together with archival *Chandra* and *XMM-Newton* observations, probe the ICM properties from the subcluster cores out to their viral radii. Previous studies of other (non-merging) systems have found entropy profiles that flatten at large radii, in contradiction with theoretical predictions, possibly due to the presence of unresolved cool gas clumps (Walker et al. 2013b; Urban et al. 2014). This behavior shows some variation with azimuth, suggesting a connection with large-scale structure and gas accretion (Ichikawa et al. 2013; Sato et al. 2014). We use our observations, which extend both along and perpendicular to the putative large-scale structure filament, to look for correlations between the ICM properties, the surrounding large-scale environment, and to examine the merger dynamics. This paper is organized as follows. In Section 2, we describe the *Suzaku*, *Chandra*, and *MMT* data used in our analysis. In Section 3, the analysis of the X-ray and optical observations is described in detail. In Section 4, we discuss systematic errors that are relevant to the *Suzaku* X-ray measurements at large radii. In Sections 5–7 we discuss our results and we present our conclusions in Section 8. Throughout the paper, a standard ΛCDM cosmology with $H_0 = 70$ km s^{-1} Mpc^{-1}, $\Omega_\Lambda = 0.7$, and $\Omega_M = 0.3$ is assumed. In this cosmology, $1'$ at the redshift of the cluster corresponds to $\sim$96.9 kpc. Unless otherwise stated, reported errors correspond to 90% confidence intervals.

2. OBSERVATIONS AND DATA PROCESSING

2.1. Optical Spectroscopic and Photometric Data

The majority of the galaxy spectroscopic redshifts used in this analysis are new observations obtained using the Hectospec instrument (Fabricant et al. 2005) at the MMT Observatory 6.5 m telescope on Mt. Hopkins, AZ. A single Hectospec configuration places up to 300 fibers in a region of the sky approximately one degree in diameter. We use data from two such configurations, which resulted in 517 individual spectroscopic redshift measurements.

To supplement our Hectospec spectroscopy, we include data from the literature, when available. Specifically, we use 12 spectroscopic redshift measurements from Huchra et al. (1995), 68 from Donnelly et al. (2001), 7 from Gal et al. (2003), 19 from the 6dF Galaxy Survey (Jones et al. 2005), and 200 from the Sloan Digital Sky Survey (SDSS; Ahn et al. 2014). The SDSS selection includes all objects within a $0\fdg5$ radius of the centroids of the X-ray emission of A1750N, A1750C, and A1750S, and with a spectroscopic redshift falling in the interval $0.03 < z_{\rm spec} < 0.15$, which easily captures the range of recessional velocities of galaxies associated with A1750. We then check for duplicate entries across the different input redshift catalogs, resulting in 24 removals and a final data set of 799 spectroscopic redshifts.

In addition to optical spectroscopy, we also use optical photometry from the SDSS catalogs. We perform a query of all objects classified as galaxies within a $0\fdg5$ radius of the centroid of the X-ray surface brightness of each subcluster and download all of the available optical photometry—in the *ugriz* bands—for those sources.

2.2. Suzaku *X-Ray Observations*

A1750 was observed with *Suzaku* with five pointings during 2011 July and December (see Table 1). We process the unfiltered *Suzaku* data with HEASOFT version 6.13, and the latest calibration database CALDB as of 2014 May. The raw event files are filtered using the FTOOL *aepipeline*. In addition to the standard filtering performed by *aepipeline*,[10] we require an Earth elevation angle $>5°$, a geomagnetic cutoff rigidity of >6 GV/c, and exclude data collected during passages through the south Atlantic anomaly as described in Bautz et al. (2009). The data taken with 3×3 and 5×5 clocking modes are

---

[10] http://heasarc.gsfc.nasa.gov/docs/suzaku/processing/criteria_xis.html

merged and the corners of the chips illuminated by the Fe-calibration sources are excluded from further analysis. We carefully examine each light curve after the initial screening to ensure that the data are free from background flaring events. Due to the increase in charge injection in data taken with XIS1 after 2011 June 1, the two rows adjacent to the standard charge-injected rows are removed.[11] The region lost due to a putative micrometeorite hit on XIS0 is also excluded from our analysis. The net exposure times of each XIS0, XIS1, and XIS3 pointing after filtering are given in Table 1. Due to our strict filtering, 30 ks of the total exposure time was lost. The total filtered *Suzaku* XIS0/XIS1/XIS3 exposure time is 250.1/250.1/250.2 ks.

2.3. Chandra X-Ray Observations

The *Chandra* observations that were used in the analysis are summarized in Table 1. For each observation, the aimpoint was on the front-side illuminated ACIS-I CCD. All data were reprocessed from the level 1 event files using CIAO 4.6 and CALDB 4.4.7. CTI and time-dependent gain corrections were applied. LC_CLEAN was used to check for periods of background flares.[12] The mean event rate was calculated from a source-free region using time bins within 3σ of the overall mean, and bins outside a factor of 1.2 of this mean were discarded. There were no periods of strong background flares. To model the background we used the CALDB[13] blank sky background files appropriate for this observation, normalized to match the 10–12 keV count rate in our observations to account for variations in the particle background. The total filtered ACIS-I exposure time is 75.9 ks.

3. ANALYSIS

3.1. Photometric Selection of Cluster Member Galaxies

SDSS *ugriz* photometry samples the full optical spectral energy distribution (SED) for galaxies in A1750, including the 4000 Å break that is located in the *g* band at the redshift of A1750. The 4000 Å break is a strong feature, characteristic of the passive red sequence (RS) galaxies that dominate the galaxy populations of evolved galaxy clusters (Gladders & Yee 2000). We identify candidate cluster member galaxies of A1750 using the RS in the *gri* bands, which span the break. The RS selection involves two steps. The initial selection is made in color–magnitude space ($g - r$ versus r; Figure 1 top panel) with a manual identification of the overdensity of galaxies with approximately the same $g - r$ color. We then perform a linear fit in color–magnitude space to define the RS in A1750, and flag all galaxies within ± 0.125 in $g - r$ magnitudes as candidate RS galaxies. The second step occurs in color–color space ($g - r$ versus $r - i$; Figure 1 bottom panel), where we identify an overdensity of candidate RS galaxies with similar $r - i$ colors.

Galaxies that satisfy the initial color–magnitude selection while also falling within ± 0.125 mag of the mean $r - i$ color of the overdensity in color–color space are flagged as RS galaxies. The range of color values that we use accounts for both the observed intrinsic scatter in the RS of massive galaxy clusters ($\sim \pm 0.05$–0.1 mag; De Lucia et al. 2004; Gladders & Yee 2005;
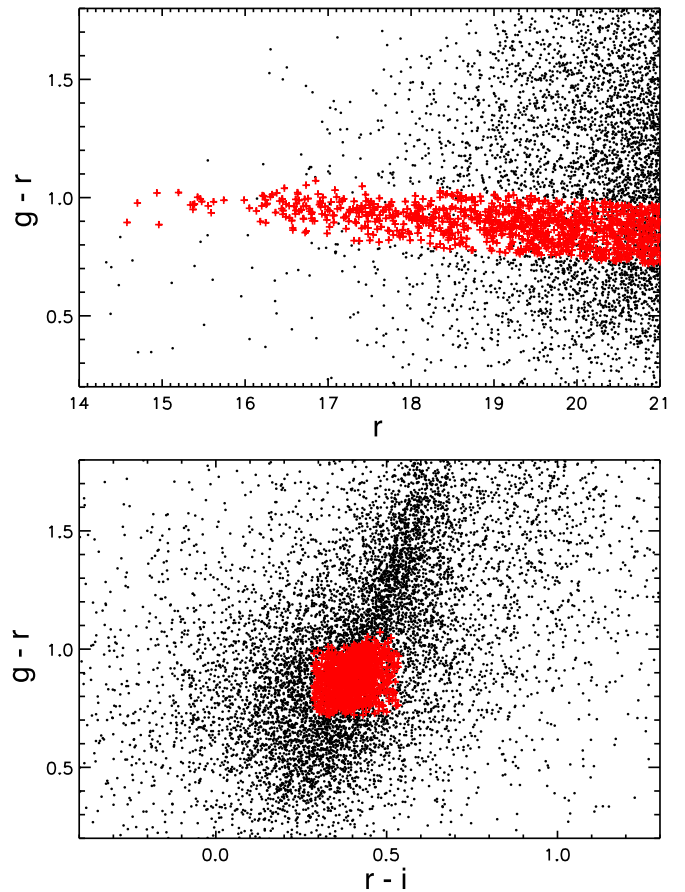
---

[11] http://heasarc.gsfc.nasa.gov/docs/suzaku/analysis/nxb_ci6kev.html
[12] http://asc.harvard.edu/contrib/maxim/acisbg/
[13] http://cxc.harvard.edu/caldb/

Figure 1. Upper panel: color–magnitude ($g - r$ vs. r) plot of galaxies included in the spectroscopic catalog, with selected passive cluster members plotted in red. Lower panel: color–color ($g - r$ vs. $r - i$) plot of galaxies included in the spectroscopic catalog, with selected passive cluster members plotted in red.

Valentinuzzi et al. 2011) and the typical SDSS photometric uncertainties of $\sim$0.025 mag.

3.2. Suzaku X-Ray Analysis

We extract an image of A1750 in the 0.5–7 keV energy band and mosaic the pointings in sky coordinates. The non-X-ray background (NXB) images are generated using the "night-Earth" data (NTE) using the FTOOL *xisnxbgen* (Tawa et al. 2008). The NXB images are then subtracted from the mosaicked image prior to exposure correction.

To generate the exposure maps, we first simulate a monochromatic photon list assuming a $20'$ uniform extended source for each observation with the XRT ray-tracing simulator *xissim* (Ishisaki et al. 2007). These vignetting-corrected photon lists are then used with *xisexpmapgen* to generate exposure maps of each pointing, as described in detail in Bautz et al. (2009). Regions with <15% of the maximum exposure time are removed. The resulting exposure maps for each pointing are merged. The particle background subtracted, vignetting-corrected image is shown in Figure 2 (left panel).

To detect X-ray point sources unresolved by *Suzaku*, we use the three *Chandra* pointings of the cluster, which overlap with the northern, central, and southern *Suzaku* pointings. The locations of the point sources in the field of view (FOV) are detected using CIAO's *wavdetect* tool and are shown in the right panel of Figure 2. Since the point-spread function (PSF)
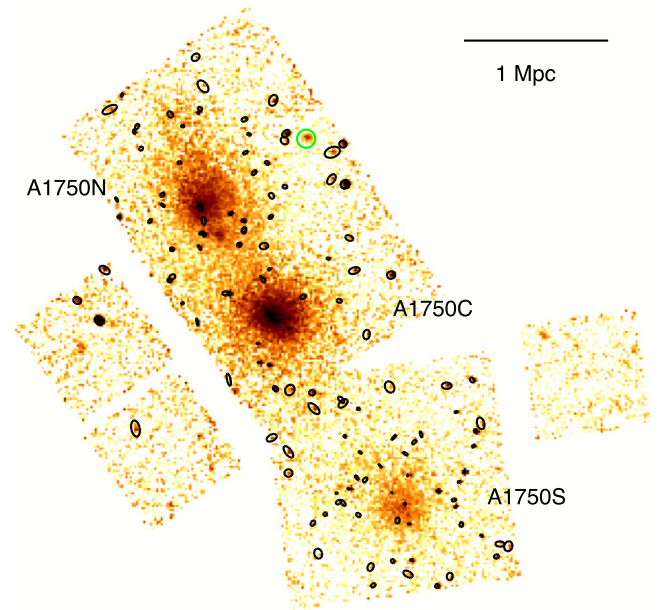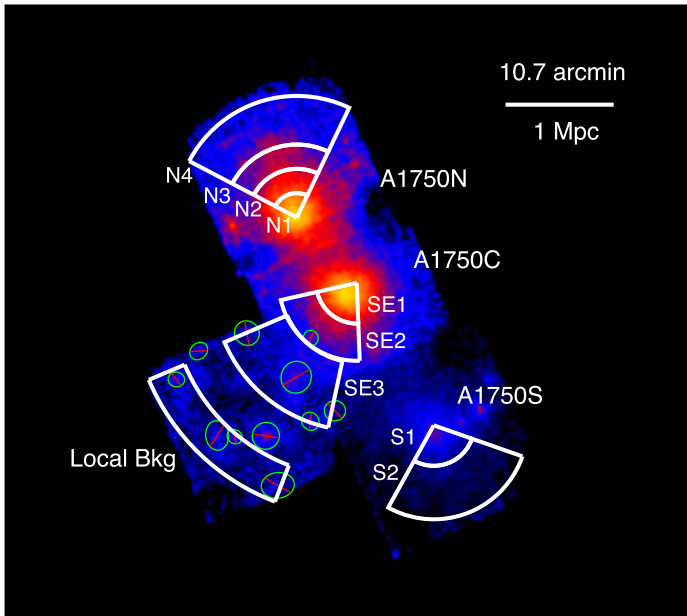
Figure 2. Left panel: exposure-corrected, NXB background-subtracted *Suzaku* XIS image of the A1750 merger system. The image was extracted in the 0.5–7 keV energy range. The spectral extraction regions are shown in white. Point sources in the southeast pointing where we lacked *Chandra* observations are shown in green. Right panel: exposure-corrected, background-subtracted *Chandra* image of A1750. The three *Chandra* pointings coinciding with the *Suzaku* observations were used to identify the coordinates of the point sources in the *Suzaku* field of view. The brightest point source, which is in both *Suzaku* and *Chandra* fields of view, is shown in green.

sizes of *Suzaku* and *Chandra* are different, the extents of the point sources reported by *wavdetect* cannot be used directly to exclude point source in the *Suzaku* FOV. We use the following procedure to determine a reliable and conservative radius for point source exclusion. The brightest point source within both the *Chandra* and *Suzaku* FOV (J2000; R.A.: 202°.603, decl.: −1°.808) is selected as a test case (shown with green circle in Figure 2 left panel). The source is located in a fairly faint region (9′ away from the center of A1750 to northeast). The *Chandra* spectrum of the point source is extracted using CIAO's *specextract* tool and is fitted with an absorbed power-law model with an index fixed to 1.4 (the slope associated with the X-ray background spectrum at 0.5–8 keV; e.g., Hickox & Markevitch 2006), while the normalization is left free. Based on the best-fit power-law index and normalization (5.22 × 10^{-6} photons keV^{-1} cm^{-2} s^{-1}) obtained from the *Chandra* fits, a 120 ks long *Suzaku*/XIS observation is simulated using the *xissim* tool. To assess the impact of the source flux on the measured parameters of the diffuse emission, we add the simulated source spectrum to a typical diffuse emission spectrum with 1000 net counts. We then incrementally increase the source exclusion radius (thereby decreasing the contribution of the point source to the total emission) and examine the effect on the best-fitting parameters to the total (source plus diffuse emission) spectrum. We find that for all exclusion radii $r > 35''$ the best-fitting parameters (kT, abundance, and normalization) are not significantly affected by the point-source contribution. Since this estimate is based on the analysis of the brightest point source in a faint region, the exclusion radius for fainter point sources would be smaller. We note that since all our spectral extraction regions include at least 2000 total counts, this radius represents a conservative estimate. We

therefore exclude regions with radii of $35''$ around point sources detected by *Chandra* from our *Suzaku* analysis.

The southeast *Suzaku* pointing does not have an overlapping *Chandra* observation. Therefore, the point sources in this region are detected from the *Suzaku* data using CIAO's *wavdetect* tool. The detection is performed using *Suzaku*'s half-power radius of 1′ as the wavelet radius, as done in Urban et al. (2014). The point sources detected with *Suzaku* are shown as green regions in the left panel in Figure 2.

Spectra are extracted from the filtered event files in *XSELECT*. Corresponding detector redistribution function (RMF) files are constructed using the *xisrmfgen* tool, while the ancillary response function (ARF) files are constructed using the *xisarfgen* tool assuming a uniform surface brightness in a 20′ radius. Cutoff-rigidity-weighted particle-induced background spectra are extracted from the NTE data for each detector using the *xisnxbgen* tool. The particle-induced background spectrum is subtracted from each source spectrum prior to fitting. Spectral fitting is performed in the 0.5–7 keV energy band where *Suzaku*/XIS is the most sensitive.

The cluster emission is modeled with an absorbed single temperature thermal plasma *apec* model with ATOMDB version 2.0.2 (Smith et al. 2001; Foster et al. 2012). *XSPEC* v12.8.2 is used to perform the spectral fits (Arnaud 1996) with the extended *C*-statistic as an estimator of the goodness of fits. We co-add front-illuminated (FI) XIS0 and XIS3 data to increase the signal-to-noise ratio, while the back-illuminated (BI) XIS1 data are modeled simultaneously with the FI observations due to the difference in energy responses. We adopt the solar abundance table from Anders & Grevesse (1989). The galactic column density is frozen at the Leiden/Argentine/Bonn (LAB) Galactic HI Survey value (Kalberla et al. 2005) of 2.37×10^{20} cm^{-2} in our fits.

We examine the local X-ray background emission using the *ROSAT* All Sky Survey (RASS) data extracted from a 1° to 2° annulus surrounding the central subcluster's centroid.[14] A region 19′–21′ away from the central subcluster A1750C in the southeast pointing is used to extract the local background (see Figure 2). The RASS spectrum is simultaneously fit with the local background XIS FI and BI spectra using two Gaussian models for solar wind charge exchange at 0.56 and 0.65 keV, an unabsorbed *apec* model for Local Hot Bubble (LHB) emission, and an absorbed *apec* model for Galactic Halo (GH) emission (Kuntz & Snowden 2000; Bulbul et al. 2012). The abundances of these *apec* models are set to solar, while the redshifts are fixed at zero. An absorbed power-law component with a photon index of 1.4 is added to the model to include emission from unresolved extragalactic sources (primarily active galactic nucleus (AGN)). We note that statistical uncertainties in the observed local background parameters given in this section are 1σ. The best-fit temperature of the LHB component is $0.14^{+0.03}_{-0.01}$ keV, with a normalization of $3.22^{+3.94}_{-0.67} \times 10^{-6}$ cm^{-5} arcmin^2. The best-fit temperature and normalization of the GH component is $0.69^{+0.11}_{-0.09}$ keV and $1.79^{+0.78}_{-0.43} \times 10^{-7}$ cm^{-5} arcmin^2. The normalization for the CXB power-law component is $5.84^{+1.50}_{-0.63} \times 10^{-7}$ photons keV^{-1} cm^{-2} s^{-1} arcmin^{-2} at 1 keV, corresponding to a CXB flux of $(1.15 \pm 0.30) \times 10^{-11}$ erg s^{-1} cm^{-2} deg^{-2}. The flux $(6.22 \pm 0.16) \times 10^{-12}$ erg s^{-1} cm^{-2} deg^{-2} in the 0.5–2 keV band is in agreement with the value $(7.7 \pm 0.4 \times 10^{-12}$ erg s^{-1} cm^{-2} deg^{-2}) reported by (Bautz et al. 2009).

4. SYSTEMATIC ERRORS ON X-RAY OBSERVABLES

In studies of low surface brightness emission, it is crucial to estimate the contribution of various systematic uncertainties, particularly those related to background modeling, to the total error budget. We consider the following potential sources of systematic error in our analysis: (i) uncertainties due to stray light contamination and the large size of the PSF of *Suzaku*'s mirrors; (ii) uncertainties due to intrinsic spatial variations in the local soft background; (iii) systematics associated with the NXB; and (vi) uncertainties due to the intrinsic spatial variation of unresolved point sources.

4.1. Scattered Light due to Large PSF

Due to *Suzaku*'s relatively large PSF, some X-ray photons that originate from one particular region on the sky may be detected elsewhere on the detector. The PSF spreading in each direction is calculated by generating simulated event files using the ray-tracing simulator *xissim* (Serlemitsos et al. 2007). *Chandra* X-ray images of each annular sector (shown in Figure 2 left panel) and the best-fit spectral models obtained from the *Suzaku* observations are used to simulate event files with 1×10^6 photons. The fraction of photons that are spread into the surrounding annuli is calculated for each XIS detector and annulus sector. Relative contributions are weighted by the effective area at 1.5 keV of each detector to calculate the overall percentage contribution (given in Table 2). We find that the majority of photons originating in an annulus on the sky are detected in the same annulus (except region N1) on the detector. Up to 15% of the photons may be detected in

surrounding annuli. However, the percentage fraction of photons that scatter into the outermost annuli at R_{200}[15] to the north and southeast from the bright cores is small ($<1\%$). These results are consistent with the photon fractions reported in Bautz et al. (2009) and Walker et al. (2012b).

Considering the shallow temperature distribution of A1750 measured by *Chandra* observations, the PSF is expected to have a minimal effect on the measurements of temperature in the outermost regions. To estimate the effect of PSF spreading on our temperature and normalization measurements, we jointly fit the spectra of sectors with *apec* models, with the normalizations scaled according to the fractions listed in Table 2. In all cases, the change in best-fit parameter values due to scattered flux from other annuli is significantly less than the statistical errors on the measured observables (see Table 9).

4.2. Systematics Related to Soft, Cosmic, and Particle X-Ray Background

To model the soft X-ray foreground and cosmic X-ray background, we jointly fit *ROSAT* RASS data with local XIS background spectra, as described in detail in Section 3.2. We find that the local X-ray background is consistent with the RASS data. However, spatial variations in the background level can introduce additional systematic uncertainties on X-ray observables. To estimate the effect of these uncertainties, we perform 10,000 Monte Carlo realizations of the background model. The model parameters are allowed to vary simultaneously within their 1σ uncertainty ranges obtained from the joint RASS local background fit. A variation of up to ~3.6% of the NXB level is also taken into account (Tawa et al. 2008). The percent systematic uncertainty contributions due to the variance in cosmic, local, and particle background on the temperature estimates are given in Table 3. We find that the effect on temperature and normalization is negligible (~1%) and smaller than the statistical uncertainties in the inner regions (shown in Table 9), while it can be as large as 25% in the outskirts near R_{200}. These uncertainties are included in the total error budget in our analysis by adding them in quadrature.

4.3. Systematics Related to Cosmic X-Ray Background

The intrinsic variations in the unresolved CXB component can be an important source of uncertainty in the analyses of cluster outskirts with *Suzaku*. To estimate the magnitude of this component, we follow a similar approach to that described in Walker et al. (2012c). The *Suzaku* data alone allow us to detect point sources to a limiting flux of 1.3×10^{-14} erg cm^{-2} s^{-1} deg^{-2} in our observations.

The contribution of unresolved point sources to the total flux in erg cm^{-2} s^{-1} deg^{-2} can be estimated as (Moretti et al. 2003)

$$F_{\mathrm{CXB}} = (2.18 \pm 0.13) \times 10^{-11} - \int_{S_{\mathrm{excl}}}^{S_{\mathrm{max}}} \frac{dN}{dS} \times S \, dS. \quad (1)$$

The source flux distribution in the 2–10 keV band is described by the analytical function

$$N(>S) = N_0 \left[\frac{(2 \times 10^{-15})^\alpha}{S^\alpha + S_0^{\alpha-\beta}} \right] \mathrm{erg\ cm^{-2}\ s^{-1}}, \quad (2)$$

---

[14] http://heasarc.gsfc.nasa.gov/cgi-bin/Tools/xraybg/xraybg.pl

[15] The overdensity radius R_{200} is defined as the radius within which the average matter density of the cluster is 200 times the critical density of the universe at the cluster redshift.

Table 2
Contribution of the Flux from the Adjacent Annuli due to PSF Spreading and Stray Light

Region	N1	N2	N3	N4	SE1	SE2	SE3	S1	S2
N1	40.88	15.64	1.41	0.45	⋯	⋯	⋯	⋯	⋯
N2	7.82	56.23	15.95	1.11	⋯	⋯	⋯	⋯	⋯
N3	1.18	15.95	58.37	13.58	⋯	⋯	⋯	⋯	⋯
N4	0.07	0.57	8.54	55.84	⋯	⋯	⋯	⋯	⋯
SE1	⋯	⋯	⋯	⋯	56.64	7.86	0.05	⋯	⋯
SE2	⋯	⋯	⋯	⋯	10.81	61.54	2.20	⋯	⋯
SE3	⋯	⋯	⋯	⋯	0.45	4.65	57.16	⋯	⋯
S1	⋯	⋯	⋯	⋯	⋯	⋯	⋯	60.78	14.35
S2	⋯	⋯	⋯	⋯	⋯	⋯	⋯	9.05	69.38

Note. Values given are the percentage contribution. Regions in different rows refer to the annulus receiving the flux, while columns are the annuli providing the flux. N—north, S—south, and SE—southeast. The regions are shown in Figure 2.

Table 3
Systematic Soft, Cosmic, and Particle X-Ray Background Uncertainties

Pointing	Region 1	Region 2	Region 3	Region 4
North	1	4	8	19
Southeast	0.7	3.4	25	⋯
South	4	20	⋯	⋯

Note. Values are the percentile systematic uncertainties on temperature for each region due to soft Galactic, cosmic X-ray, and the particle background.

where $N_0 = 5300^{+2850}_{-1400}$, $S_0 = (4.5^{+3.7}_{-1.7}) \times 10^{-15}$, $\alpha = 1.57^{+0.10}_{-0.18}$, and $\beta = 0.44^{+0.12}_{-0.13}$. We then integrate Equation (1) from a lower limit of $S_{excl} = 1.3 \times 10^{-14} \, \mathrm{erg \, cm^{-2} \, s^{-1}}$ (the flux of the faintest source in our FOV) up to the upper limit of $S_{max} = 8.0 \times 10^{-12} \, \mathrm{erg \, cm^{-2} \, s^{-1}}$ (Moretti et al. 2003). The integration gives an unresolved 2–10 keV flux of $(1.20 \pm 0.43) \times 10^{-11} \, \mathrm{erg \, cm^{-2} \, s^{-1} \, deg^{-2}}$.

The expected deviation in the CXB level due to unresolved point sources is

$$\sigma_B^2 = \frac{1}{\Omega} \int_0^{S_{excl}} \frac{dN}{dS} \times S^2 \, dS, \qquad (3)$$

where Ω is the solid angle (Bautz et al. 2009). Using the power-law relation (given in Equation (2)) in Equation (3), we calculate the 1σ rms fluctuations in the CXB (given in Table 4). We find that the variation is $4.3 \times 10^{-12} \, \mathrm{erg \, cm^{-2} \, s^{-1} \, deg^{-2}}$ in the faintest outermost SE3 region, which extends to R_{200}. These estimates are consistent with the values reported by Bautz et al. (2009) and Hoshino et al. (2010). The 1σ uncertainty on the measured CXB (from joint RASS and local background fits) is comparable to the expectation value of fluctuations on the CXB brightness calculated here. We include this variation in our Monte Carlo Markov realizations of the X-ray background to account for the CXB variation (as described in detail in Section 4.2). The final systematic errors on the observed quantities were added in quadrature.

5. OPTICAL PROPERTIES AND MERGER DYNAMICS

In this section, we describe our search for substructure in the optical data and use it to further constrain the dynamical state and merger history of A1750 and determine whether the subclusters are bound to each other.

Table 4
Estimated 1σ Fluctuations in the CXB Level due to Unresolved Point Sources in the *Suzaku* FOV in Units of $10^{-12} \, \mathrm{erg \, cm^{-2} \, s^{-1} \, deg^{-2}}$

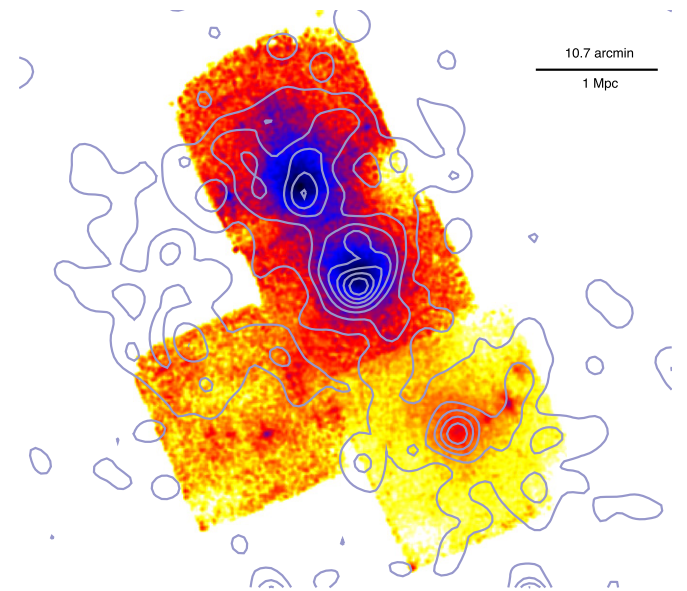| Pointing	Region 1	Region 2	Region 3	Region 4
North	17.6	10.2	7.9	4.4
Southeast	11.1	6.8	4.3	⋯
South	9.9	4.7	⋯	⋯

Figure 3. *Suzaku* X-ray image of the A1750 merger system with contours from the smoothed optical red light distribution overplotted in blue.

5.1. The RS Galaxy Population

In Figure 3 we overplot the spatial density of RS galaxies on the sky on the *Suzaku* X-ray image. This map is created from a cloud-in-cell interpolation of the spatial distribution of RS selected galaxies on the sky, where galaxies are weighted by their *r*-band magnitudes (brighter galaxies weighted more heavily). The resulting map of the surface density of RS light traces the collisionless galaxy component of the system. We then applied a broad Gaussian smoothing kernel of 54″ to generate the contours shown in the image.

The peaks observed in the red light distribution roughly align with the peaks in the X-ray emission. We note that we do not find strong evidence for extended filaments along the axis of the aligned clumps in RS light, and thus no large-size groups

Table 5
Cluster Member Dynamics

Region	N_{mem}	z_{med}	σ_{1D} (km s^{-1})	Δv^{a} (km s^{-1})
Total System	243	0.0861 ± 0.0028	780 ± 30	0
A1750N	25	0.0832 ± 0.0006	750 ± 160	-810
A1750C	40	0.0864 ± 0.0004	835 ± 120	90
A1750S	33	0.0868 ± 0.0019	532 ± 60	200

Note.
[a] Peculiar velocity relative to the recession velocity of the entire merging system.

are detected along the filament direction to the north. The lack of evidence indicates that the filaments do not contain significant large group-like structures with a detectable RS population.

5.2. Spectroscopic Properties of Cluster Member Galaxies

The large sample of spectroscopic redshifts available in the A1750 field provides an opportunity to investigate the dynamical state of cluster member galaxies. We first characterize the cluster member dynamics for the entire system by making an initial selection of cluster members that are within a projected physical radius of 1 Mpc of the centroid of the X-ray emission of each subcluster (this is approximately equal to the region covered by our Hectospec observations), and which have redshifts in the interval $0.07 < z < 0.1$. We then use the biweight location and scale estimators (Beers et al. 1990) as the starting guess for the median and dispersion of cluster member velocities. We then iterate this process, rejecting galaxies with redshifts more than 3-σ away from the median until the redshift sample converges. This results in an estimate of the velocity dispersion for the entire system of $\sigma_v = 780 \pm 30$ km s^{-1}, and a median redshift of $\bar{z} = 0.0861 \pm 0.0002$ (a recession velocity, $\bar{v} = 23780 \pm 50$ km s^{-1}) based on 243 cluster member redshifts.

Given that we have hundreds of spectroscopic cluster members, we can also test for line of sight velocity differences between the three individual X-ray subclusters. We define subsets of spectra that originate from galaxies located in three non-overlapping 3′ radius circular regions on the sky that are centered on the X-ray peaks of each of the three distinct subclusters. For each of these regions, we use all of the cluster member galaxies that satisfy the $\pm$3-σ velocity range for the total cluster system from above, and compute the biweight location and scale estimates of the median and dispersion in the galaxy velocities. These regions extend out radially $\sim$300 kpc from each X-ray centroid, and therefore only include a relatively small fraction of the full sample of 243 cluster member spectra (between 25 and 40 cluster members per subregion).

The resulting kinematics estimates are given in Table 5; the central and southern X-ray clumps have redshifts that are similar to the median for the total system, but the northern clump is blueshifted, with a peculiar velocity of -810 km s^{-1} (see Figure 4). The observed peculiar velocities imply that any relative motion between the central and southern clumps is in the plane of the sky, while the northern clump is moving at least partly along a vector that is normal to the sky.
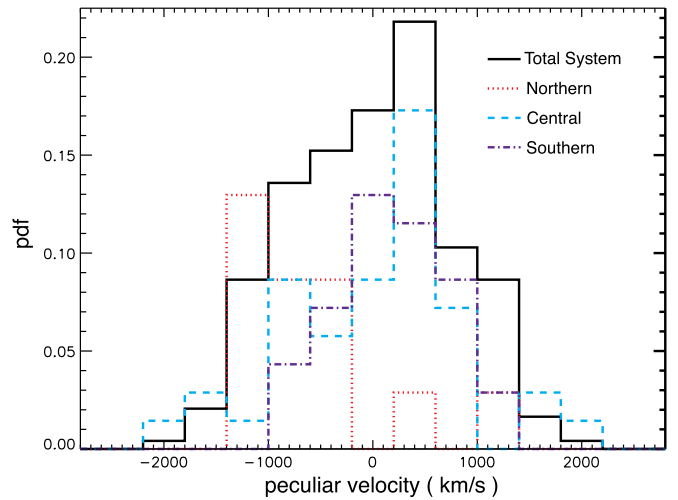

Figure 4. Histograms of the velocity distribution of galaxies that sample the subclusters and the merger superstructure. Values of the biweight median and variance are listed in Table 5.

The velocity dispersion of galaxies within the total structure is not larger than the velocity dispersion of the individual clumps, indicating that the system is unrelaxed. The individual subclusters have not begun to virialize into the final larger cluster, i.e., the total mass of all three clumps is $\sim 10^{15}$ $M_{\odot}$, and 840 km s^{-1} is well below the velocity dispersion of a virialized structure of that mass. The shape of the velocity distributions within the different subcluster regions (plotted in Figure 4), suggest that northern and central subclusters are less well structured (with asymmetric velocity dispersion profiles) than the southern subcluster. This could be due to some degree of interaction between the central and northern subclusters, while the southern subcluster may still be infalling (i.e., has not started tidally interacting with the other systems).

We further calculated the implied virial masses of individual subclusters based on the velocity dispersions. Using the Evrard et al. (2008) scaling relations, the virial masses of A1750N, A1750C, and A1750S are $4.6^{+3.6}_{-2.4} \times 10^{14}$ $M_{\odot}$, $6.4^{+3.1}_{-2.4} \times 10^{14} M_{\odot}$, and $1.7^{+0.6}_{-0.5} \times 10^{14} M_{\odot}$, respectively. These masses are consistent with total masses of each subcluster obtained from X-ray observations (see Section 7.1 for detailed calculations).

5.3. A Dynamical Model for the A1750N–A1750C System

We apply a dynamical model introduced by Beers et al. (1982) and Andrade-Santos et al. (2015) to evaluate the dynamical state of the subclusters A1750N and A1750C. This model allows us to estimate the most likely angle between the merger axis and the plane of the sky.

The equations of motion take two different forms, depending on whether the subclusters are gravitationally bound or not. For the case where they are gravitationally bound, we parameterize the equations of motion in the following form:

$$R = \frac{R_m}{2}(1 - \cos \chi), \qquad (4)$$

$$t = \left(\frac{R_m^3}{8GM}\right)^{1/2} (\chi - \sin \chi), \qquad (5)$$

$$V = \left(\frac{2GM}{R_m}\right)^{1/2} \frac{\sin\chi}{(1-\cos\chi)}, \qquad (6)$$

where R_m is the subclusters' separation at the moment of maximum expansion, M is the system's total mass, and χ is the variable used to parametrize Friedmann's equation, also known as the development angle. For the case of non-gravitationally bound subclusters, the equations are parameterized as

$$R = \frac{GM}{V_\infty^2}(\cosh\chi - 1), \qquad (7)$$

$$t = \frac{GM}{V_\infty^3}(\sinh\chi - \chi), \qquad (8)$$

$$V = V_\infty \frac{\sinh\chi}{(\cosh\chi - 1)}, \qquad (9)$$

where V_∞ is the velocity of expansion at the asymptotic limit. V_r, the radial velocity difference, and R_p, the projected distance, are related to the parameters of the equations by

$$V_r = V\sin\alpha, \quad R_p = R\cos\alpha, \qquad (10)$$

where α is the projection angle of the system with respect to the plane of the sky.

The virial mass of these subclusters is $M = (7.2 \pm 1.0) \times 10^{14}\,M_\odot$ (sum of the masses of both subclusters within R_{200}—uncertainties is quoted here as 68% confidence intervals; see Section 7.1 for detailed calculations) derived from Bulbul et al. (2010) ICM models. We assume that the subclusters' velocities are the median velocities of their galaxies. The projected distance on the plane of the sky between the X-ray center of each subcluster is $R_p = 0.93$ Mpc. The difference of the median redshifts of these subclusters yields a radial velocity difference of $V_r = 884 \pm 199\,\mathrm{km\,s^{-1}}$. By setting $t = 12.4$ Gyr, the age of the universe at the mean redshift of these subclusters ($z = 0.0848$), we close the system of equation. The parametric equations are then solved via an iterative procedure, which computes the radial velocity difference V_r for each projection angle α.

Using simple energy considerations, we determine the limits of the bound solutions:

$$V_r^2 R_p \leqslant 2GM\sin^2\alpha\cos\alpha. \qquad (11)$$

Figure 5 presents the projection angle (α) as a function of the radial velocity difference (V_r) between the subclusters. The uncertainties in the measured radial velocity and mass of the subclusters lead to a range in the solutions for the projection angles (α_{inf} and α_{sup}). We compute the relative probabilities of these solutions by

$$p_i = \int_{\alpha_{inf,i}}^{\alpha_{sup,i}} \cos\alpha\,d\alpha, \qquad (12)$$

where each solution is represented by the index i. We then normalize the probabilities by $P_i = p_i/\left(\sum_i p_i\right)$.

Solving the parametric equations we obtain two bound solutions and one unbound solution. For the case of the bound solutions, the subclusters are either approaching each other at $931\,\mathrm{km\,s^{-1}}$ (22% probability) or at $2186\,\mathrm{km\,s^{-1}}$ (78% probability). The former solution corresponds to a collision in less than 3.1 Gyr, given their separation of ~ 2.97 Mpc. The latter corresponds to a collision in less than 460 Myr, given their separation of ~ 1017 kpc. The unbound solution (0.02%
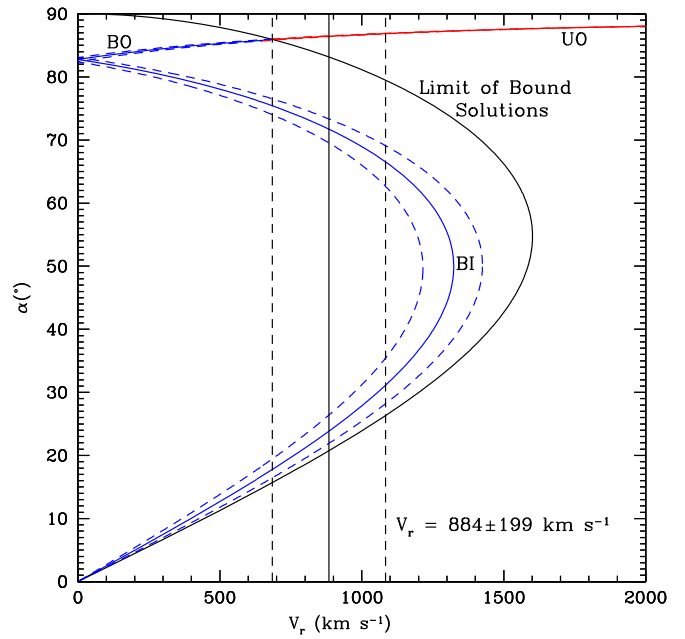

Figure 5. Projection angle (α) as a function of the radial velocity difference (V_r) between the subclusters. UO, BI, and BO stand for Unbound Outgoing, Bound Incoming, and Bound Outgoing solutions. Solid red and blue lines correspond to unbound and bound solutions, respectively. The vertical solid line corresponds to the radial velocity difference between the median velocities of the galaxies in each subcluster. Dashed lines correspond to 68% confidence ranges.

Table 6
Best-fit Parameters for the Bound Incoming Solutions of the A1750N–A1750C System

χ (rad)	α (degrees)	R (kpc)	R_m (kpc)	V (km s^{-1})	P (%)
4.542	71.73	2966.7	5072.2	931.2	22
5.319	23.86	1016.9	4727.4	2186.2	78

Note. Columns list best-fit values for χ and α for the bound solutions of the dynamical model, and the corresponding values for R, R_m, V, and the probability of each solution.

Table 7
Best-fit Parameters for the Unbound Outgoing Solution of the Dynamical Model of the A1750N–A1750C System

χ (rad)	α (degrees)	R (kpc)	R_m (kpc)	V (km s^{-1})	P (%)
1.692	86.45	15025.5	886.0	610.4	0.02

Note. Columns present best fits for the χ and α for the unbound solution, and the corresponding values for R, V, V_∞, and the probability of this solution.

probability) corresponds to a separation of ~ 15 Mpc. The parameters of these solutions are presented in Tables 6 and 7. Given its very low probability, the unbound solution can be neglected, while the bound solution in which the separation between the clusters is ~ 1017 kpc is highly favored (78% probability).

As mentioned in Andrade-Santos et al. (2015), the method to determine the dynamical state of a system of clusters from Beers et al. (1982) assumes a purely radial infall. Also, the way the probabilities are computed, by integrating over the angles determined by the uncertainties on the mass of the system,

Table 8
Best-fit Parameters for the Bound Solutions of the A1750C–A1750S System

χ (rad)	α (degrees)	R (kpc)	R_m (kpc)	V (km s^{-1})	P (%)	Relative Motion
2.871	77.68	7871.0	8017.1	113.0	10	Outgoing
3.385	74.76	6390.7	6486.5	114.4	15	Incoming
4.987	4.39	1684.9	4620.9	1442.4	75	Incoming

Note. Columns list best-fit values for χ and α for the bound solutions of the dynamical model, and the corresponding values for R, R_m, V, and the probability of each solution.

favors small angle solutions. Therefore, the probabilities for the solutions should be treated with caution, as we have no information about the angular momentum of this subclusters.

5.4. A Dynamical Model for the A1750C–A1750S System

Now we apply the same procedure to determine the dynamical state of the pair A1750C–A1750S. Using the virial mass estimated from the velocity dispersion of the galaxies in the southern subcluster, the total mass of this system is $M = (6.5 \pm 1.7) \times 10^{14} \, M_\odot$ (uncertainties are quoted here at the 68% confidence level). The difference between the median redshifts of these subclusters yields a radial velocity difference of $V_r = 110 \pm 123 \, \mathrm{km \, s^{-1}}$. Solving the system of parametric equations (Equations (4)–(10)) yields the results presented in Table 8, with A1750C–A1750S being bound in all solutions. The most likely solution (75% probability) indicates that the merger is happening very close to the plane of the sky ($\alpha = 4°$), also supporting the scenario in which all three subclusters are merging along a cosmic filament.

6. THE OBSERVED ICM PROPERTIES

We extract spectra in concentric annular sectors along the north (filament), south (filament), and southeast (off-filament) directions from the regions shown in Figure 2. Each spectral extraction region is selected to include at least 2000 net source counts. The LHB+CXB+GH components are fixed to the values determined from fits to the local background and RASS data as described in Section 3.2. We stress that the systematic errors are included as explained in Section 4. The *Suzaku* spectra are fitted using an absorbed single temperature (1T) *apec* model with free temperature, abundance, and normalization.

6.1. Filament Direction

We first examine the *Suzaku* spectra extracted along the north direction starting from the center of A1750N. The spectra are extracted from four consecutive annular sectors; $0'$–$2'.5$, $2'.5$–$5'$, $5'.0$–$7'.5$, and $7'.5$–$12'.5$. The total source counts in the co-added FI observations in regions N1, N2, N3, and N4 are 3300, 4400, 2700, and 3300, respectively. The BI spectra in the same regions have total source counts of 2400, 3300, 2100, and 2600. Both FI and BI spectra of the outermost $7'.5$–$12'.5$ region are dominated by the NXB background at >6 keV, and thus this band is excluded from further analysis.

To investigate the nature of the gas along the filament, we first fit the FI and BI spectra simultaneously with a 1T *apec* model. The parameters of the FI and BI spectral models are tied to each other. The abundances are only constrained by the

Table 9
Best-fit Parameters of the 1T *apec* Model

Region	kT (keV)	Abund ($A_\odot$)	$\mathcal{N}$ (10^{-6} cm^{-5})	C-Stat (dof)
N1	$3.33^{+0.17}_{-0.14}$	0.28 ± 0.5	110.18 ± 2.95	178.10 (177)
N2	$2.80^{+0.16}_{-0.20}$	0.15 ± 0.4	48.87 ± 1.70	183.31 (244)
N3	1.98 ± 0.18	0.2^a	17.55 ± 0.77	272.86 (165)
N4	1.61 ± 0.30	0.2^a	6.08 ± 1.09	322.35 (241)
S1	2.61 ± 0.21	0.19 ± 0.08	22.28 ± 1.79	148.68 (144)
S2	$2.04^{+0.30}_{-0.41}$	$0.20^{+0.24}_{-0.14}$	2.76 ± 1.15	201.25 (187)
SE1	$4.72^{+0.17}_{-0.13}$	0.31 ± 0.01	154.79 ± 5.33	712.29 (746)
SE2	4.83 ± 0.40	0.2^a	31.93 ± 1.44	776.43 (747)
SE3	$2.47^{+0.75}_{-0.68}$	0.2^a	4.26 ± 1.10	495.63 (473)

Note.
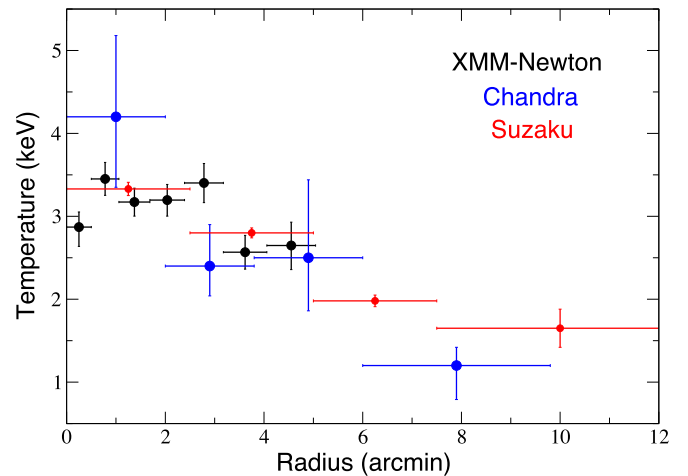^{a} Indicates the fixed parameters.

Figure 6. Comparison of projected temperatures of A1750 to the north direction obtained from *Suzaku* (in red), *Chandra* (in blue), and *XMM-Newton* observations (in black; Belsole et al. 2004). The 1σ error bars of *XMM-Newton* and *Suzaku* temperatures include systematic and statistical uncertainties. Temperatures reported by three satellites are in a good agreement. We are able to extend the gas temperature measurements out to 0.9 R_{200} of A1750N ($R_{200} \sim 14'$) and R_{200} of A1750C ($R_{200} \sim 16'$) clusters.

observations in regions N1 and N2. The best-fit temperatures are $3.33^{+0.17}_{-0.14}$ keV and $2.80^{+0.16}_{-0.20}$ keV, respectively. A 1T *apec* model produces an acceptable fit to the spectra of the innermost two regions. Adding an additional *apec* model does not significantly improve the fits for these regions. The model parameters are given in Table 9.

A 1T *apec* model produces best-fit temperatures of 1.98 ± 0.18 keV and 1.61 ± 0.30 keV in regions N3 and N4, respectively. Abundances are not constrained; we therefore assume an abundance of 0.2 $A_\odot$, as observed in the outskirts of low-mass clusters (Walker et al. 2012b). The projected temperature profile to the north is shown in Figure 6. We compare the *Suzaku* results with those from *Chandra* (this work) and *XMM-Newton* (Belsole et al. 2004). We note that the *Chandra* results shown in Figure 6 do not include the systematic uncertainties, and are shown here for a rough check on the *Suzaku* temperature estimates. We find good agreement between measurements from each satellite. We note that both *Suzaku* and *Chandra* observations cover the radial range out to 0.9 R_{200} ($\sim 14'$, see Section 7.1), and the best-fit temperatures measured by *Suzaku* and *Chandra* are in agreement at the 1σ
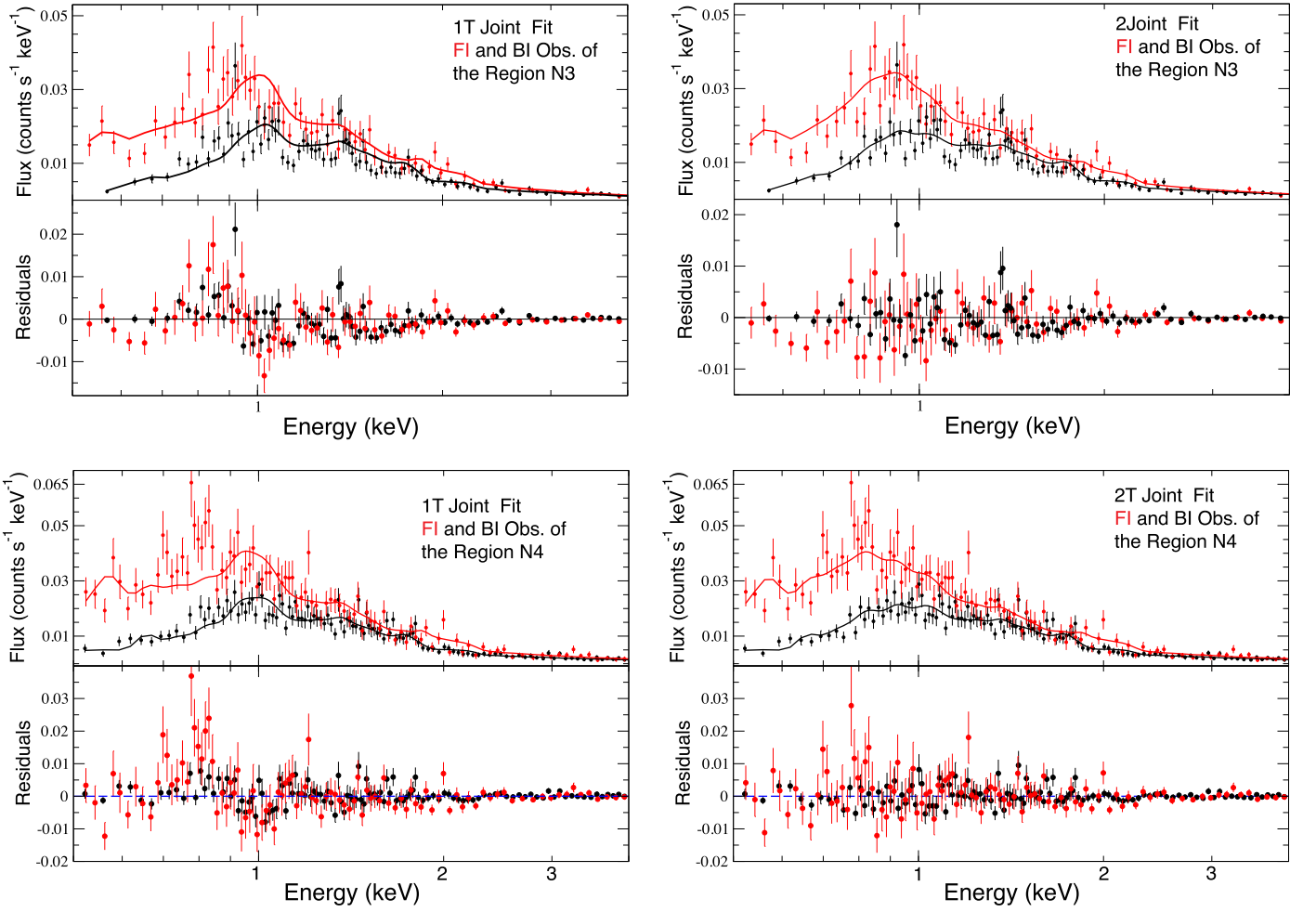
Figure 7. Left panel: single temperature thermal model fit to the *Suzaku* joint FI (in red) and BI (in black) spectra extracted from the region N3 and N4 along the filament direction to the north (shown in Figure 2). The best-fit model parameters obtained from this fit are given in Table 9. Residuals <2 keV indicate the probability of a secondary softer thermal component. Right panel: 2T *apec* model fit to the joint *Suzaku* FI and BI spectra. The best-fit parameters of the fit are given in Table 10. The change in $\Delta\chi^2$(N3, N4) = (28.5, 24.4) for an extra two degrees of freedom suggests that the detection of a softer thermal component with ∼1 keV along the filament direction toward north is significant.

Table 10
The Best-fit Parameters of the 2T *apec* Model in Regions N3 and N4 in the 0.5–7 keV Energy Band

Region	kT_1 (keV)	Abund ($A_\odot$)	$\mathcal{N}_1$ (10^{-6} cm^{-5})	kT_2 (keV)	$\mathcal{N}_2$ (10^{-6} cm^{-5})
N3	$3.24^{+1.40}_{-0.55}$	0.1[a]	10.32 ± 2.05	$1.01^{+0.13}_{-0.07}$	$9.19^{+2.42}_{-1.82}$
N3	$2.93^{+0.57}_{-0.40}$	0.2[a]	11.76 ± 1.66	0.99 ± 0.07	$4.87^{+1.56}_{-1.04}$
N3	$2.93^{+0.46}_{-0.37}$	0.3[a]	11.75 ± 1.53	0.95 ± 0.08	$3.29^{+0.92}_{-0.68}$
N4	$1.95^{+0.62}_{-0.39}$	0.1[a]	$4.81^{+1.09}_{-1.72}$	$0.79^{+0.19}_{-0.10}$	2.98 ± 0.71
N4	$2.12^{+0.50}_{-0.37}$	0.2[a]	$4.53^{+1.05}_{-1.01}$	0.81 ± 0.12	1.74 ± 0.36
N4	$2.29^{+0.50}_{-0.40}$	0.3[a]	4.21 ± 1.33	$0.80^{+0.12}_{-0.08}$	1.28 ± 0.25

Note.
[a] Values held constant.

confidence level. However, since *Suzaku* has a lower background at large radii (∼R_{200}) and more precise temperature measurements (i.e., smaller systematic+statistical uncertainties), we will use *Suzaku* temperature and density measurements hereafter.

The residuals in the spectrum after a model fit in the softer 0.5–2.0 keV band (shown in the left panel of Figure 7) suggest the possible presence of a second, cooler thermal component in the regions N3 and N4. To investigate this, we add another

absorbed *apec* component to the model (2T) and redo the fit. Both the temperature and the normalization of the second component are left free, while the abundances are tied to each other between the two *apec* models. The best-fit parameters of the 2T *apec* model and the improvement in the fits are given in Table 10. Figure 7 (right panel) shows the improvements in the fits of both region N3 and N4. The temperature of the primary *apec* component increases from 1.98 ± 0.09 keV to $2.93^{+0.57}_{-0.40}$ keV, while the temperature of the secondary

Region	kT_1 (keV)	$\mathcal{N}_1$ (10^{-6} cm^{-5})	kT_2 (keV)	$\mathcal{N}_2$ (10^{-6} cm^{-6})
N$_3$	1.96 ± 0.18	$16.45^{+0.72}_{-0.74}$	...	...
N$_3$	$2.90^{+0.85}_{-0.66}$	10.82 ± 2.19	$0.99^{+0.08}_{-0.10}$	4.75 ± 1.21
N$_3$	1.59 ± 0.29	5.73 ± 1.12	...	...
N$_4$	$2.09^{+0.69}_{-0.51}$	$4.22^{+1.13}_{-1.16}$	$0.79^{+0.17}_{-0.13}$	1.73 ± 0.44

component is estimated to be 0.99 ± 0.07 keV in region N3. The change in the goodness of the fit statistics is significant, with a ΔC-Statistic of 64.5 for an additional two degrees of freedom (dof). The C-Statistic value does not provide a statistical test to quantify the significance of the improvement in the fit from adding the second component, thus we calculate the corresponding χ^2 values before and after addition of the secondary *apec* model. We find that adding two dof (additional temperature and its normalization) improves the χ^2 by 28.5. In region N4, the best-fit temperature of the primary *apec* becomes $2.12^{+0.50}_{-0.37}$ keV in the 2T *apec* fits, while the temperature of the secondary component is 0.81 ± 0.12 keV. The $\Delta \chi^2$ value of 24.4 with an additional two dof, corresponding to a null hypothesis probability of $\sim 10^{-6}$, suggests that the detection is significant. The best-fit parameters of these 2T models are summarized in Table 10. The derived *XSPEC* normalizations, i.e., emission measures, and temperatures depend on the assumed metallicity. We provide the measurements of these observables for various solar abundance fractions. We note that the assumed metallically does not have a significant impact on temperature or emission measure of the hotter component in our fits. The discussion of the nature of this gas is provided in Section 6.1.

Considering that the calibration of XIS below 0.7 keV is uncertain, we re-perform the 1T and 2T model fits in the N3 and N4 regions to investigate the effect of this uncertainty on the temperature and normalization (i.e., density). Fixing the abundance at $0.2 \ A_\odot$, we find that the temperatures and normalizations of both models are consistent with results from the 0.5–7 keV band fits within the total (statistical plus systematic) uncertainties. The results from the 1T and 2T model fits in the 0.7–7 keV band are given in Table 11. We conclude that the detection of the cooler ~ 1 keV gas is not significantly affected by the effective area uncertainties below 0.7 keV.

To investigate the X-ray emission along the filament to the south, we extract spectra from two annular sectors (regions S1 and S2) extending south from the center of A1750S. These regions are shown in Figure 2. Region S1 extends from the cluster core to 4′, and region S2 extends from 4′ to 9′.7. The source counts in the combined FI and BI observations are 2600 and 1700 in region S1, and 2200 and 2000 in region S2. We first fit the spectra with a 1T *apec* model. The best-fit temperatures of 2.61 ± 0.21 keV and $2.04^{+0.30}_{-0.41}$ keV, and abundances of $0.19 \pm 0.08 \ A_\odot$ and $0.20^{+0.24}_{-0.14} \ A_\odot$ are measured in regions S1 and S2, respectively. The results are shown in Table 9 with the goodness of the fits. Abundance measurements of $0.2 \ A_\odot$ are consistent with the abundances measured in low-mass systems (Walker et al. 2012c). The possible presence of the cool ~ 1 keV gas is tested by performing 2T *apec* fits. The additional secondary *apec* model does not

significantly improve the fits. Unlike the detection in the north, we find no evidence for such a component in the south.

6.2. Off-filament Direction

The X-ray emission to the southeast, perpendicular to the putative large-scale filament, is examined using spectra extracted in annular sectors (SE1, SE2, and SE3 shown in Figure 2) with radii of 0′–4′, 4′.0–8′.0, and 8′ extending out to R_{200} ($\sim 16'$) of the central subcluster. The total source counts in the FI and BI observations are 7800 and 5000 in region SE1, and 4000 and 2600 in region SE2, and 3000 and 2500 in region SE3.

To study the nature of the gas along the off-filament direction we followed a similar approach to that outlined in Section 6.1. The FI and BI spectra of each region are first fit with a 1T *apec* model. The best-fit parameters and the goodness of these fits are given in Table 9. The temperature and abundance in the innermost region are $4.72^{+0.17}_{-0.13}$ keV and $0.31 \pm 0.01 \ A_\odot$. The best-fit temperature of the SE2 region is 4.83 ± 0.40 keV. Unlike in region SE1, we are not able to constrain the abundance in region SE2; thus, the abundance parameter is fixed at $0.2 \ A_\odot$. To test if the best-fit temperature is sensitive to the assumed metallicity, we perform the fit with abundances of $0.1 \ A_\odot$ and $0.3 \ A_\odot$. The best-fit temperature declines to 4.73 ± 0.39 keV for an assumed abundance of $0.1 \ A_\odot$, while it increases to 4.95 ± 0.38 keV for an abundance of $0.3 \ A_\odot$. However, the change in the measured temperature is not statistically significant.

The spectrum from region SE3 are dominated by the NXB above 5 keV. Therefore, we perform our fits in the 0.5–5 keV energy band in this region. The best-fit temperature is $2.47^{+0.75}_{-0.68}$ keV for an assumed abundance of $0.2 \ A_\odot$. The temperature is $2.56^{+0.67}_{-0.70}$ keV and $2.85^{+0.78}_{-0.74}$ keV for fixed abundances of $0.1 \ A_\odot$ and $0.3 \ A_\odot$, respectively. The temperatures for our assumed abundances are all consistent within the 1σ level. In all cases, we observe a significant sharp decline in the projected temperature at $\sim R_{500}$ (10′.6; see Section 7.1) to the southeast.

Taking a similar approach as in Section 6.1, we fit the spectra of the outermost regions SE2 and SE3 with a 2T *apec* model. The temperature of the secondary component is not constrained, and this addition does not improve the fit significantly. Thus, we find no evidence for a softer thermal component in the off-filament direction. To further test if the ~ 1 keV gas detected along the filament to the north is observable along the off-filament southeast direction, we scale the normalization of the softer component detected in region N4 (see Table 10) by the ratio of the area of regions SE3 and N4. Freezing the normalization to the scaled value of 1.5×10^{-5} cm^{-5} and the observed temperature to 0.99 keV, we refit the FI and BI spectra of the SE3 region. The temperature and normalizations of the primary component are unconstrained after the fit is performed. The sharp decline in the goodness of the fit (C-Statistics value of 4931.15 for 471 dof) suggests that if the ~ 1 keV gas detected along the filament direction existed in this region with the same surface brightness, it would be detected. Thus, this component is clearly absent in the off-filament direction.
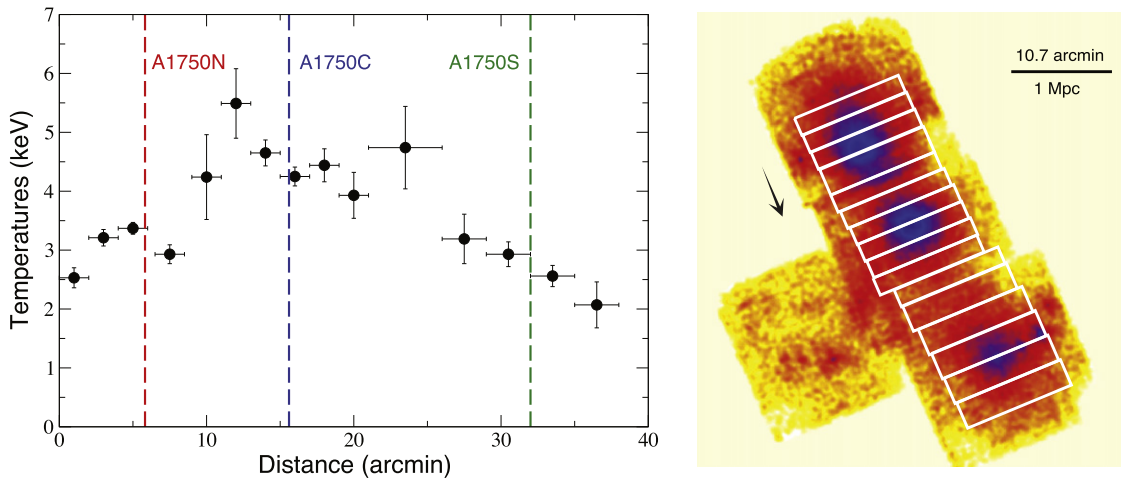
Figure 8. Left panel: projected temperature measured from *Suzaku* observations as a function of radial distance along the filament axis. The dashed lines indicate the centroids of the subclusters A1750N, A1750C, and A1750S. Right panel: an image of the mosaicked *Suzaku* observations of the A1750 merger system. The spectral extraction regions are indicated in white. The selection of the regions is defined along the line connecting the centroids of the three subclusters. The direction is indicated with an arrow.

6.3. ICM between the Sub-clusters

We investigate the distribution of the gas temperature between A1750N–A1750C and between A1750C–A1750S along the merger axis. We define rectangular regions along the line connecting the centroids of the three subclusters (Figure 8, right), which are marked with dashed lines in Figure 8 (left panel). We fit the spectra of the selected regions using a 1T *apec* model. Figure 8 (left panel) displays the projected temperature as a function of distance. We find that, starting from the northernmost region, the temperature keeps rising toward the center of A1750N, and reaches a peak temperature of 3.37 ± 0.10 keV. Due to the large PSF of *Suzaku*, we cannot rule out or confirm the suggestion that A1750N is a cool-core cluster (Donnelly et al. 2001; Belsole et al. 2004). Continuing past A1750N, the temperature rises up to 5.49 ± 0.59 keV with a sharp increase at $\sim 6'$ (~ 0.5 Mpc). This increase in the temperature is significant at a level of 2.7σ. Hot, presumably shock-heated gas between A1750N and A1750C, coinciding with the location where we detect hot gas with *Suzaku*, has previously been observed in *Chandra* and *XMM-Newton* data (Belsole et al. 2004; Molnar et al. 2013). The presence of hot gas in this region is an indication of an interaction between the A1750N and A1750C subclusters.

A1750C shows a relatively uniform temperature around the centroid, with a peak temperature of 4.25 ± 0.16 keV. We detected another temperature peak located $7'$ away from A1750C, in the southwest direction, with a temperature of 4.74 ± 0.70 keV. Southwest of this peak, the temperature declines to 3.19 ± 0.42 keV. This sharp decrease is significant at a 4σ level, suggesting an interaction between the subclusters A1750S and A1750C. A hot region, where the peak detected by *Suzaku* observations, was previously detected in the vicinity of A1750C (Belsole et al. 2004). Due to large error bars on the temperature ($5.7^{+1.9}_{-1.7}$ keV), the authors were unable to determine the true nature of the structure and claimed that it could due to a point source. Similarly a hot region was observed in *Chandra* data (Molnar et al. 2013) coinciding with the reported location of the peak. Here we confirm the extended nature of the emission and suggest a potential interaction between A1750C and A1750S. However, we note that the optical data

do not show any evidence of interaction between these clusters (see Section 5.2 for discussion).

The projected temperature continues to decline toward the center of the southern subcluster A1750S. The central temperature of A1750S is 2.93 ± 0.21 keV. The radial temperature profile shows that the temperature decreases smoothly moving across the center of A1750S toward the southwest.

7. DEPROJECTED ICM PROPERTIES

To examine the radial profiles of cluster masses and thermodynamical quantities such as entropy and pressure, we determine the deprojected density and temperature. The electron density is obtained from the best-fit normalization $\mathcal{N}$ of the *apec* model in *XSPEC* using the relation,

$$\mathcal{N} = \frac{10^{-14}}{4\pi \, D_A{}^2 (1 + z)^2} \int n_e(r) n_H(r) dV \text{ cm}^{-5}, \quad (13)$$

where D_A is the angular size distance to the source in units of cm, and n_e and n_H are the electron and hydrogen number densities in units of cm^{-3}. We note that the ARFs generated by *xissimarfgen* assume a uniform source occupying an area of 400π square arcminutes. We therefore apply a correction factor to each region and normalization prior to deprojection. An "onion-peeling" method is used to deproject the temperature and density profiles (Kriss et al. 1983; Blanton et al. 2001; Russell et al. 2008). The resulting deprojected density and temperature profiles to the north, southeast, and south directions are shown in Figure 9.

We extend the temperature and density profiles out to $0.9\,R_{200}$ for A1750N to the north and R_{200} for A1750C to the southeast with the new *Suzaku* observations (see in Figure 2). The temperature profiles to the north and southeast decline with radius and reach half of the peak value at R_{200}. Similar temperature declines have been reported for other clusters (e.g., Bautz et al. 2009; Hoshino et al. 2010). We observe a rather gradual decline in temperature to the north and south. However, the profile to the southeast indicates a uniform temperature within $8'$ and falls relatively rapidly beyond R_{2500}.
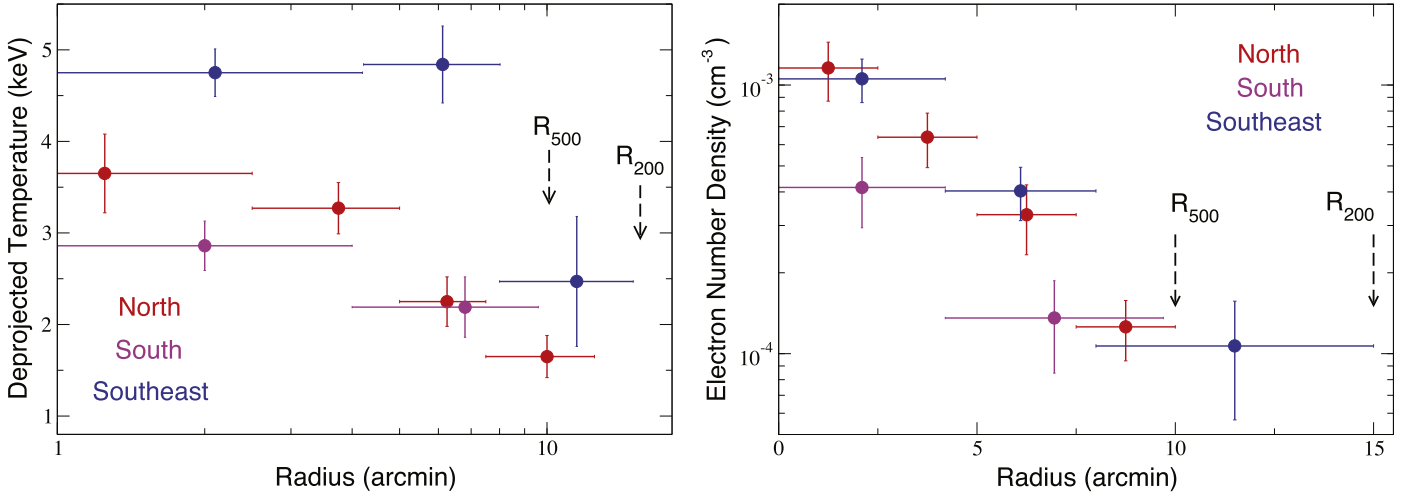
Figure 9. Deprojected temperature (left panel) and electron density (right panel) profiles of the A1750 merger system to the north, south, and southeast directions. The 90% systematic errors were added to the total error budget. The R_{500} and R_{200} estimates of A1750C are indicated with arrows.

7.1. Mass Analysis

Based on the average deprojected density and temperature, we estimated the mass of each subcluster within R_{500} using the $T_X - M_{tot}$ scaling relation (Vikhlinin et al. 2009, V09 hereafter). The spectra between $0.15-1R_{500}$ are extracted to determine the global properties for each cluster. To avoid flux contamination, adjacent subclusters were excluded.

A1750N has a best-fit global temperature of $3.14^{+0.08}_{-0.07}$ keV, and an abundance of $0.15 \pm 0.03 \, A_\odot$. Our measurement is consistent with the temperature of 3.17 ± 0.1 keV reported in Belsole et al. (2004). The scaling relation predicts a total mass of $1.98 \times 10^{14} M_\odot$ at R_{500} (9'.3). The best-fit temperature of A1750C is $4.15^{+0.12}_{-0.07}$ keV, with an abundance of $0.21^{+0.03}_{-0.02} \, A_\odot$. The global temperature reported in Belsole et al. (2004) is slightly lower ($kT = 3.87 \pm 0.10$ keV). Their extraction region excludes the hotter plasma between A1750N and A1750C, which may account for the difference observed in temperature. The V09 scaling relation predicts a total mass of $3.03 \times 10^{14} M_\odot$ enclosed within R_{500} (10'.6). The spectral fit to A1750S gives a best-fit temperature of $3.59^{+0.20}_{-0.17}$ keV and an abundance of $0.20^{+0.07}_{-0.06}$. The estimated total mass within R_{500} (9'.9) is $2.43 \times 10^{14} M_\odot$.

To investigate the radial behavior of the gas mass, the total mass, and the gas mass fraction, we employ a physically motivated ICM model described in Bulbul et al. (2010, 2011, B10, hereafter). The B10 model is based on the assumption that the ICM is a polytropic gas in hydrostatic equilibrium in the cluster's gravitational potential. The deprojected density and temperature profiles are fit simultaneously using the B10 model. The fitting was performed using a Markov Chain Monte Carlo (MCMC) approach, with Metropolis–Hastings sampling, to determine posterior distributions for the best-fit model parameters. The temperature profile is

$$T(r) = T_0 \left[\frac{1}{(\beta - 2)} \frac{(1 + r/r_s)^{\beta - 2} - 1}{r/r_s (1 + r/r_s)^{\beta - 2}} \right], \quad (14)$$

where the normalization constant T_0 is

$$T_0 = \frac{4\pi G \mu m_p}{k(n+1)} \frac{r_s^2 \rho_i}{(\beta - 1)}. \quad (15)$$

Using the relation between temperature and gas density provided by the polytropic relation, the gas density is

$$n_e(r) = n_{e0} \left[\frac{T(r)}{T_0} \right]^n, \quad (16)$$

where $\beta + 1$ is the slope of the total density distribution, n is the polytropic index, r_s is the scale radius, and T_0 and n_{e0} are the central temperature and density of the polytropic function. This model has sufficient fitting flexibility to describe X-ray data, while making simple physical assumptions (Bonamente et al. 2012; Bulbul et al. 2012; Hasler et al. 2012; Landry et al. 2013). We note that the core taper function in the B10 model is omitted in the fits performed in this work, since *Suzaku* observations are not able to resolve the cluster cores. Figure 10 shows the best-fit models to the density (left panel) and temperature (right panel) in the off-filament and filament directions.

Due to the limited number of data points compared to the number of free model parameters of the B10 model (five in this case), we were not able to constrain all of the free parameters of the model. The β parameter is fixed to the slope of the Navarro–Frenk–White profile (Navarro et al. 1996), while the scale radius r_s (fixed in our fits), the radius beyond which the temperature starts declining, is estimated from the temperature profiles (see Figure 10). The rest of the model parameters (n, n_{e0}, and T_{e0}) are allowed to vary independently. The best-fit parameters of the model are given in Table 12, along with the goodness of the fits. The best-fit models for the density and temperature profiles are displayed in Figure 10, with 90% confidence intervals. Given the limited number of data points, the profiles to the south are not constrained.

The total mass enclosed within radius r is

$$M(r) = \frac{4\pi \rho_i r_s^3}{(\beta - 2)} \left[\frac{1}{\beta - 1} + \frac{1/(1 - \beta) - r/r_s}{(1 + r/r_s)^{\beta - 1}} \right]. \quad (17)$$
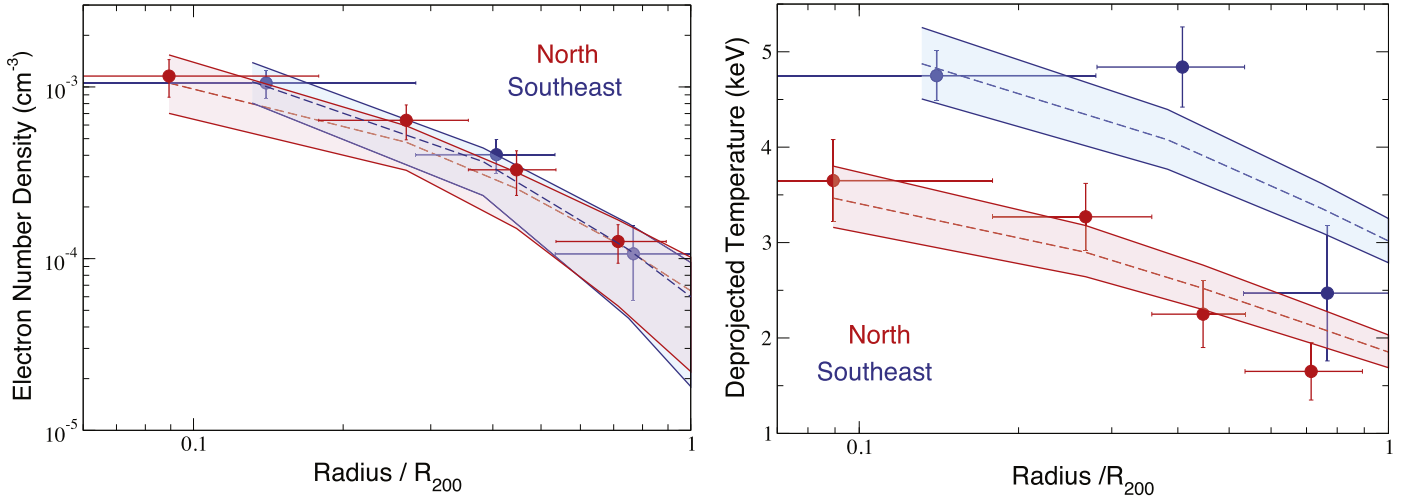
Figure 10. B10 model fits to the density (left panel) and deprojected temperature (right panel) profiles to the filament (north) and off-filament (southeast) directions. The best-fit model is shown in dashed lines, while the 90% confidence intervals are illustrated in shaded areas. The model provides an acceptable fits to the data, the goodness of the fits are given in Table 12.

Table 12
Best-fit Parameters of the B10 Model

	North	Southeast
n_{e0} ($\times 10^{-3}$ cm^{-3})	$1.78^{+0.86}_{-0.41}$	$2.19^{+0.92}_{-0.40}$
T_{e0} (keV)	3.89 ± 0.22	5.49 ± 0.27
n	$4.49^{+1.38}_{-0.52}$	$6.01^{+1.79}_{-0.62}$
r_s (arcmin)	300^*	480^*
β	2.0^*	2.0^*
χ^2 (dof)	5.35 (5)	3.21 (3)

Note. Fixed parameters are indicated with *.

The normalization factor for the total matter density is $\rho_i = [T_0 k (n + 1)(\beta - 1)]/(4\pi G \mu m_p r s^2)$.

The gas mass M_{gas} is computed by integrating the gas density profile within the volume,

$$M_{gas}(r) = 4\pi \mu_e \, m_p \int n_e(r) \, r^2 \, dr, \tag{18}$$

where μ_e and m_p are the mean molecular weight per electron and the proton mass.

The gas mass fraction is

$$f_{gas} = \frac{M_{gas}}{M_{tot}}. \tag{19}$$

The gas mass, total mass, and f_{gas} are measured at R_{500}, determined using the V09 scaling relations, and are given in Table 13. Following Pratt et al. (2010), we assume $R_{500} = 0.659 R_{200}$. The total mass, gas mass, and gas mass fraction profiles are plotted in Figure 11. We find that the total masses enclosed within R_{500} are well within agreement with the total masses estimated using the V09 scaling relations. The gas mass fractions of A1750N and A1750C are consistent with the gas mass fraction expected for clusters in this mass range based on the V09 scaling relations ($f_{gas} \sim 0.11$) at R_{500}. The B10 model was then used to calculate the masses and mass fraction at R_{200}. We found that the gas mass fraction of A1750C and A1750N at R_{200} is $0.11^{+0.10}_{-0.06}$ and $0.15^{+0.07}_{-0.06}$.

The virial masses of the A1750N and A1750C subclusters are in agreement with the mass estimates from the optical observations at a 2.7σ level (see Section 5.2). However, we

note that, the cluster mass inferred from X-ray analysis depends on the geometry of the merger, hydrostatic equilibrium, and other model parameters (e.g., scale radius) of the merging clusters.

The gas fractions derived in the filament and off-filament directions are consistent with the cosmic baryon fraction derived from *WMAP* seven-year data of 0.166 (Komatsu et al. 2011). Similarly, gas mass fractions consistent with the cosmic value, were observed in RX J1159+5531 (Humphrey et al. 2012; Su et al. 2015), A1689 (Kawaharada et al. 2010), and A1246 (Sato et al. 2014). However, we note that the total mass estimates are based on a few assumptions on the distribution of the gas properties. Spherical symmetry and isotropy are assumed when calculating these masses. Such assumptions may bias our results, particularly in a merger system at large radii.

7.2. Entropy Profiles

The entropy ($K = kT/n_e^{2/3}$) and pressure ($P = n_e kT$) profiles are calculated using the electron density (n_e) and deprojected temperature (kT). The profiles along the filament and off-filament directions are shown in Figure 12.

In the absence of non-gravitational processes, such as radiative cooling and feedback, cluster entropy profiles are expected to follow the simple power-law relation

$$\frac{K}{K_{500}} = 1.42 \, (R/R_{500})^{1.1}, \tag{20}$$

where we assume a cosmic baryon fraction of $f_b = 0.15$, with a characteristic entropy of

$$K_{500} = 106 \text{ keV cm}^{-2} \left(\frac{M_{500}}{10^{14} \, h_{70}^{-1} \, M_\odot} \right)^{2/3} \left(\frac{1}{f_b} \right)^{2/3}$$
$$\times E(z)^{-2/3} \, h_{70}^{-4/3} \text{ keV cm}^{-2}, \tag{21}$$

(Voit et al. 2005; Pratt et al. 2010). We used an M_{500} (the total mass within R_{500} of A1750C) of $3 \times 10^{14} M_\odot$, as determined in Section 7.1. The resulting expected self-similar entropy profile for A1750C is shown as the dashed lines in Figure 12 (left).

Table 13
Gas and Total Mass Estimates at R_{500} and R_{200} Obtained from B10 Model

Cluster	R_{500} (arcmin)	$M_{gas}(R_{500})$ ($10^{13}M_\odot$)	$M_{tot}(R_{500})$ ($10^{14}M_\odot$)	$f_{gas}(R_{500})$	R_{200} (arcmin)	$M_{gas}(R_{200})$ ($10^{13}M_\odot$)	$M_{tot}(R_{200})$ ($10^{14}M_\odot$)	$f_{gas}(R_{200})$
A1750N	9.′3	1.86 ± 0.38	$1.54^{+0.29}_{-0.26}$	$0.12^{+0.04}_{-0.03}$	14.′1	$3.41^{+0.97}_{-0.92}$	$2.32^{+0.43}_{-0.39}$	$0.15^{+0.07}_{-0.06}$
A1750C	10.′6	$3.15^{+0.61}_{-0.63}$	$3.04^{+0.56}_{-0.47}$	$0.10^{+0.04}_{-0.03}$	16.′2	5.46 ± 0.16	$4.85^{+1.62}_{-1.18}$	$0.11^{+0.10}_{-0.06}$
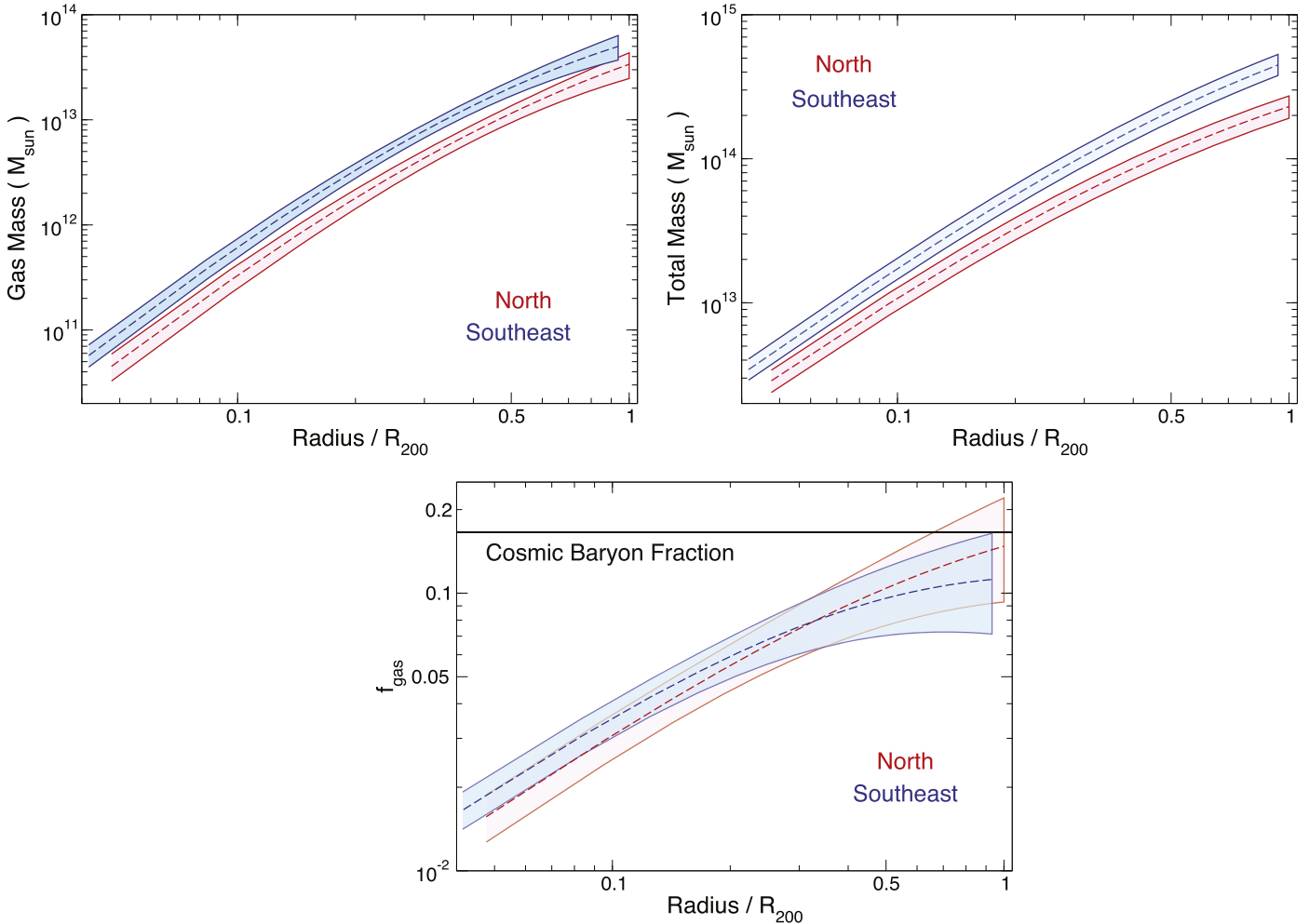
Figure 11. Gas mass, total mass, and gas mass fraction obtained from the B10 model of A1750N and A1750C subclusters. The dashed lines show the masses obtained from the best-fit models. The shaded area shows the 90% confidence interval. *Suzaku* data indicate that the gas mass fraction at R_{200} is consistent with the cosmic baryon fraction of 0.166 indicated by a solid line in the lower panel (Komatsu et al. 2011). We do not see any evidence for super-cosmic values for f_{gas} that would arise from clumping at large radii either along or perpendicular to the large-scale filamentary structure.

We find that the entropy along the filament directions (to the north and south) and off-filament direction derived from *Suzaku* data alone are in good agreement with each other within $<0.3 \, R_{200}$. Profiles obtained from *XMM-Newton* observations are consistent with those from *Suzaku* data within $<0.2 \, R_{200}$. The observed entropy exceeds the self-similar model prediction within $<0.5 \, R_{200}$, which we attribute to the influence of non-gravitational processes (e.g., AGN feedback, infalling sub-structures due to violent merging events) in the subcluster cores. Such an influence on the entropy profiles of a sample of low-redshift clusters ($z < 0.25$) was reported by Walker et al. (2012a).

The entropy profiles follow a flatter profile beyond a radius of $\sim0.3 \, R_{200}$, and become consistent with the self-similar model, both along the northern filament and off-filament directions. We find that the entropy profile toward the northern filament reaches the self-similar level at smaller radii ($\sim0.4 \, R_{200}$) as compared with the off-filament direction. This may be due to the lower temperature gas (~1 keV) observed to the north, which biases the average temperature low, and depresses the measured value of the entropy. The entropy profile along the off-filament direction stays above the self-similar expectation to $\sim0.5 \, R_{200}$. Beyond this radius it remains consistent with the self-similar prediction. If the entropy contribution from the cool gas detected to the north is removed, the entropy rises to 1245.6 ± 486.5 keV cm^2 (shown in Figure 12 with the dashed data point in red) and becomes more consistent with the entropy to the southeast. This provides evidence that the cool
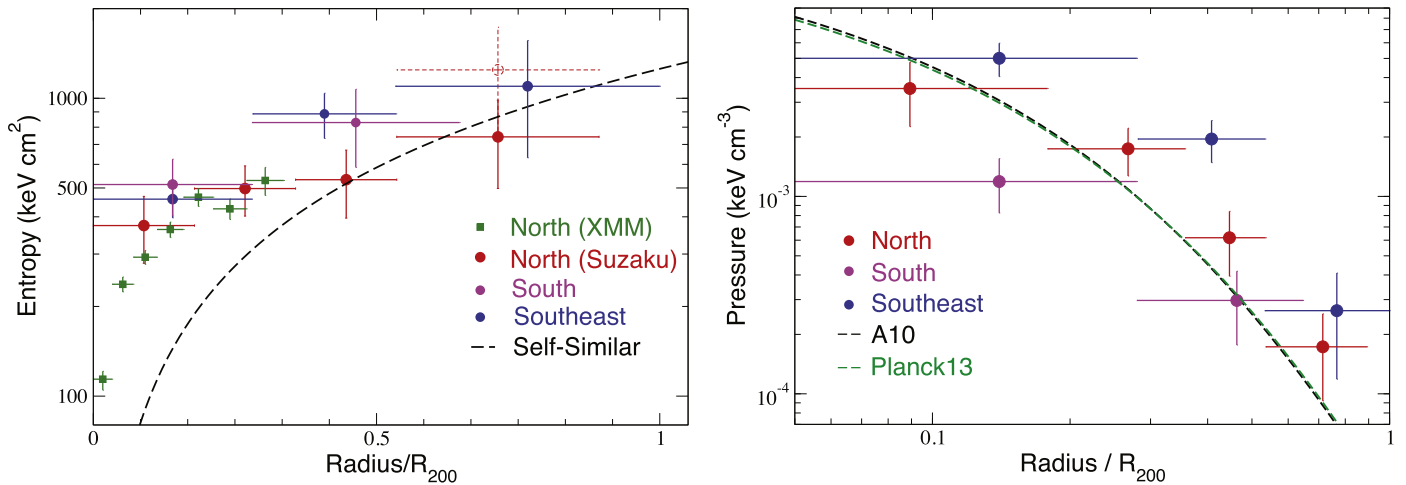
Figure 12. Left panel: entropy profile in the filament (to south and north), and off-filament (to southeast) directions. *XMM-Newton* observations are plotted in green squares to the north are in good agreement with the *Suzaku* observations (Belsole et al. 2004). The dashed line indicates the self-similar expectation (Voit et al. 2005; Pratt et al. 2010). The entropy exceeds the self-similar model within the inner $\sim$0.5 R_{200} and follows the expectation beyond this radius. The entropy becomes more consistent when the contribution from the cool gas detected to the north is removed. The entropy of the hotter component is shown with a data point in red with dashed lines. Right panel: pressure profiles in the filament, and off-filament directions. The universal Arnaud et al. (2010) and Planck Collaboration et al. (2013a) profiles are shown in black and green dashed lines, respectively. Both profiles are scaled to the estimated R_{200} of each subcluster.

gas does indeed lead to a slight decrease in the entropy, although not at the level seen in other systems where it is likely arises from gas clumping (Urban et al. 2014).

Unlike the rising, self-similar entropy observed in A1750, a flattening of entropy profiles near R_{200} appears to be a common feature in other relaxed and disturbed clusters (for a review, see Reiprich et al. 2013). A few detailed studies of nearby bright merging systems have probed the physical properties of the ICM at large radii. For the nearby bright merging Coma cluster (Simionescu et al. 2013) find no evidence for entropy flattening along the relatively relaxed directions, although due to large uncertainties they are unable to exclude entropy flattening at the level of what is observed in some relaxed clusters. The authors suggested that the gas clumping may be smaller in the outskirts of the Coma Cluster than in cool-core clusters, or the gas clumps may be more easily destroyed in dynamically active clusters. From *XMM-Newton* observations of the dynamically young, cool Virgo cluster, (Urban et al. 2011) found that the entropy profile was suppressed beyond 450 kpc by a factor of 2–2.5 below the expectation from pure gravitational collapse models. They attributed this flattening to gas clumping at large radii.

There has been great effort in the literature to explain the seeming ubiquity of flattened entropy profiles at large radii. In the hierarchical model of structure formation, clusters form by accreting material from their surrounding large-scale structure. Accretion of infalling subhalos can cause gas motions and "clumpiness" around R_{200}. These subhalos tend to have lower temperature and higher density than the surrounding ICM, leading to a bias toward lower temperatures and higher densities in the emission measure-weighted spectra, if the subhalos are unresolved. The level of gas inhomogeneities is characterized through the clumping factor ($C = \langle n_e^2 \rangle / \langle n_e \rangle^2$). As a result of overestimation of density, the gas mass and subsequently the gas mass fraction are biased high (i.e., above the cosmic baryon fraction). The observed excess in the gas mass fraction (M_{gas}/M_{tot}) in the *Suzaku* observations of the

Perseus cluster was explained with a very large clumping factor of three to four around R_{200} (Simionescu et al. 2011).

Nagai & Lau (2011) reported that the expected clumpiness factor at R_{200} can be as large as two and confirmed the flattened entropy profiles beyond $r > 0.5 R_{200}$ in their non-radiative and cooling+star formation simulations. However, Walker et al. (2012a) examined entropy profiles for a sample of relaxed clusters at $z < 0.25$ out to R_{200} and concluded that the gas clumping calculated in the numerical simulations is insufficient to reproduce the observed flattening of the entropy.

An alternative explanation to the flattening was proposed by Hoshino et al. (2010) and Akamatsu et al. (2011), and is based on the electron–ion non-equilibrium in the cluster outskirts. If the energy is not transferred to the electrons through electron–ion collisions sufficiently rapidly, the electron temperature remains low compared to that of ions, leading to an apparent entropy suppression at R_{200}.

Lapi et al. (2010) and Cavaliere et al. (2011) proposed that the flattening in the entropy is a result of a weakened accretion shock as it expands. The bulk energy carried along with the shock increases the turbulence and non-thermal pressure support in the outskirts, but the shock is not energetic enough to raise the intracluster entropy. The decreasing thermalization in low-density regions results in a tapered entropy around $\sim R_{200}$. This claim supports the observed azimuthal variations in entropy in cool-core clusters (Ichikawa et al. 2013) and in the non-cool-core Coma cluster (Simionescu et al. 2013). Other proposed explanations of entropy flattening include a rapid radial fall of the gas temperature caused by non-gravitational effects (Fusco-Femiano & Lapi 2014) and cosmic-rays consuming as a significant sink for the kinetic energy in the outskirts (Fujita et al. 2013).

On the other hand, Eckert et al. (2013) have performed a joint *Planck* SZ and *ROSAT* X-ray analysis of 18 galaxy clusters and concluded that entropy profiles are consistent with a self-similar power-law increase expected from pure gravitational infall. The discrepancy between the Eckert et al. (2013) and the Walker et al. (2012a) results is due to the differing

dependence on SZ and X-ray signals to the electron pressure used to derive entropy profiles (Fusco-Femiano & Lapi 2014).

Self-similar entropy profiles at R_{200} have been previously observed in low-mass relaxed fossil groups, e.g., RX J1159 +5531 (Humphrey et al. 2012; Su et al. 2015). On the other hand, the entropy of morphologically relaxed groups has been found to be significantly higher than self-similar at $r < R_{500}$ (Sun et al. 2009). However, massive mergers ($M_{200} > 10^{14} h^{-1} M_\odot$) are expected to have a higher level of gas clumping, since they have a larger fraction of lower temperature gas that is not detectable in the X-ray band (Nagai & Lau 2011; Vazza et al. 2013). Although A1750 is a dynamically young, massive system, we do not find evidence for gas clumping in this merger system. Entropy profile measurements along the off-filament and filament directions are in agreement with each other and with the universal expectation with a power-law relation $\propto r^{1.1}$. Remarkably in A1750, the entropy profiles within R_{200} do not seem to have been influenced by the apparent filamentary structure of the system. Our results suggest that gravitational collapse is the main driver of the temperature and density profiles in the outskirts.

7.3. Pressure Profiles

We also examine the pressure profiles along the off-filament and filament directions. Pressure profiles are calculated assuming an ideal gas law with $P(r) = n_e(r)kT(r)$, and compared to the universal pressure profiles of Arnaud et al. (2010; A10, hereafter) and Planck Collaboration et al. (2013a; Planck13, hereafter) for clusters with mean redshifts of 0.11 and 0.17, respectively. The A10 universal pressure profile is

$$P(r) = 1.65 \times 10^{-3} h(z)^{8/3} \left[\frac{M_{500}}{3 \times 10^{14} h_{70}^{-1} M_\odot} \right]^{2/3+\kappa}$$
$$\times \, \mathbb{P}(r/R_{500}) \, h_{70}^2 \, \text{keV cm}^{-3}, \qquad (22)$$

where the scaled pressure profile is characterized based on the generalized Navarro–Frenk–White profile (Nagai et al. 2007)

$$\mathbb{P}(r/R_{500}) = \frac{P_0}{(c_{500} \, r/R_{500})^\gamma [1 + (c_{500} \, r/R_{500})^\alpha]^{(\beta-\gamma)/\alpha}}, \qquad (23)$$

and

$$\kappa = \alpha_p + \alpha'_p (r/R_{500})$$
$$= (a_p + 0.10) - (a_p + 0.10) \frac{(r/0.5 \, R_{500})^3}{1 + (r/0.5 \, R_{500})^3}, \quad (24)$$

with best-fit parameters of $P_0 = 8.403 \, h_{70}^{-3/2}$, $c_{500} = 1.177$, $\gamma = 0.3081$, $\alpha = 1.0510$, and $\beta = 5.4905$. The first term in Equation (24), α_p, is an approximation that depends on the departures from the standard scaling relations, while the second term, α'_p, represents a break from self-similarity. Since non-gravitational processes become less dominant at large radii, the latter term is negligible at $> R_{500}$. The A10 universal pressure profile primarily samples the inner regions, while the Planck13 profile samples the cluster outskirts. The pressure profiles derived from the Planck observations for a sample of 62 galaxy clusters found slightly higher pressure than that predicted by A10 in the outskirts of clusters. These profiles were obtained by averaging pressure profiles from all azimuths for a large sample of clusters with different dynamical states. The dispersion over the universal profiles can be as large as 100% at $\sim R_{500}$ (see Figure 8 in A10).

We compare the pressure profiles of A1750 with the universal profiles of A10 and Planck13 in the right panel of Figure 12. While the pressure profile along the filament direction to the north agrees with the universal profile, the profile along the off-filament direction is higher and the profile to the south is lower than the expectation within $<0.2 \, R_{200}$. On the other hand, the profile in the filament direction to the south and to the north is consistent with the A10 and Planck13 universal profiles at large radii ($\sim R_{200}$) at the 2.7σ level. The pressure to the southeast exceeds the universal models at all radii.

Pressure excesses at large radii have been previously reported in other relaxed clusters, e.g., PKS 0745–191 (Walker et al. 2012b), the Centaurus cluster (Walker et al. 2013a), and the fossil group RX J1159+5531 (Humphrey et al. 2012), and were attributed to gas clumping. Figure 9 indicates that the excess in the pressure along the southeast direction compared to the north or south directions in A1750 is due to high temperature (not high density). On the contrary, clumping (if it existed in this system) would bias the density measurements high, leading to an excess in pressure and a decrement in entropy in the outskirts. Therefore, the deviation from the universal profile in A1750 is unlikely to be due to clumpy gas, since other evidence for clumping, e.g., entropy flattening and an excess in gas mass fraction (see Section 7.1), is not observed in this system. We note that Belsole et al. (2004) reported the detection of a weak $M = 1.2$, shock resulting from a merger event intrinsic to A1750C along the southeast direction. This merger event may elevate the temperature and cause deviations from the universal profile. In any event, given the large dispersion among pressure profiles of clusters in the A10 and Planck13 samples, we do not expect the pressure profiles derived in A1750 in perfect agreement with their results.

7.4. Nature of the Cool Gas Detected to the North

The cool ~ 1 keV gas detected in regions N_3 and N_4 (see Figure 7) may be (1) the hot dense warm–hot intergalactic medium (WHIM) connecting A1750N to the large-scale filament, (2) stripped ICM gas formed as a result of infalling groups, or (3) gas stripped from A1750N itself, as it interacts with filament gas or with A1750C. The feature is relatively extended with an observed radial range of >0.62 Mpc. Assuming a geometry for the merger system, the mass of the feature can be calculated (see Section 5.3 for the detailed calculation). Assuming that the density of the feature is constant within each region ($5.56 \times 10^{-6} \, (l/1 \, \text{Mpc})^{-0.5} \, \text{cm}^{-3}$), and can be described as a cylinder that extends to 1.2 Mpc with a line of sight depth of the structure (l), we obtain a gas mass of $4.13 \times 10^{11} \, (l/1 \, \text{Mpc})^{0.5} \, M_\odot$. The observed flux of the feature (1×10^{-15} erg cm^{-2} s^{-1} arcmin^{-2}), density, and temperature (~ 0.8 keV) are consistent with the expected surface brightness and temperature of the dense portion of the WHIM, where the large-scale structure interacts with the cluster's ICM (Dolag et al. 2006; Werner et al. 2008; Planck Collaboration et al. 2013b).

Such a filamentary feature also may be due to an additional small subcluster infalling into A1750N, which is being disrupted as it interacts with the main cluster. The bulk of

the halo gas lags behind the infalling groups, and is stripped by the ram pressure of the ambient ICM. Such halos are expected to have an average temperature of ~1 keV with a typical halo mass of $3 \times 10^{13} M_\odot$ (Sun et al. 2009). Bright, large-scale (~700 kpc) stripped tails have been observed in the outskirts of galaxy clusters, e.g., the Virgo cluster (Randall et al. 2008), A85 (Ichinohe et al. 2015), and A2142 (Eckert et al. 2014). The stripped gas from infalling halos may seed gas inhomogeneities (i.e., clumping), which suppress the average entropy inferred at large radii. In such systems, a flattening of the entropy profile, as well as an excess in the gas mass fraction as compared with the cosmic value, have often been observed in cluster outskirts. In the case of A1750, the entropy profile remains consistent with the self-similar prediction out to R_{200}, and the gas mass fraction is consistent with the cosmic value (see Section 7.1), implying that the observed cool gas could indeed be the densest and hottest parts of the WHIM. In addition, dense and cool clumps in the outer cluster regions are expected to lead to more entropy flattening since they will lower the average temperature, and, more importantly raise the average density (Walker et al. 2013b). Along the north direction of A1750N, there is sufficient cool gas to be detected, but it does not cause the dramatic entropy flattening seen in some other clusters, suggesting that its density cannot be too high. Completely ruling out the ram pressure-stripping scenario for this cool gas requires deeper *Chandra* observations with good angular resolution. The WHIM interpretation of this feature cannot be firmly established based on the *Suzaku* data.

8. SUMMARY

We present an analysis of the strongly merging cluster A1750 using *Suzaku* and *Chandra* X-ray observations, and *MMT* optical observations out to the cluster's virial radius. The deep *Suzaku* observations allow us to constrain the entropy, pressure, and mass profiles at the outskirts, both along and perpendicular to the large-scale filament. We use optical observations to constrain the dynamical state of the cluster. Our major results are as follows.

1. A1750N and A1750C have a 78% chance of being bound. There is an apparent hot region with a temperature of 5.49 ± 0.59 keV in between these subclusters, implying an interaction. The red galaxy distribution and the velocity dispersion data prefer a pre-merger scenario. In an early pre-merger scenario, one expects the outer ICM atmospheres of the subclusters to interact subsonically, driving shocks, and ultimately creating a heated ICM region between the subclusters, e.g., N7619 and N7626 (Randall et al. 2009).

2. We find overall a good agreement between the measured entropy profiles and the self-similar expectation predicted by gravitational collapse near R_{200} both along and perpendicular to the putative large-scale structure filament. Unlike some other clusters, the entropy profiles at large radii, both perpendicular and along the filamentary directions, are consistent with each other. Agreement of the entropy with the self-similar expectation at R_{200} in this massive and dynamically young system suggests that A1750 exhibits little gas clumping at large radii.

3. The gas mass fractions in both the filament and off-filament directions are consistent with the cosmic baryon fraction at R_{200}. This may indicate that gas clumping may

be less common in such smaller, lower temperature ($kT \sim$ 4 keV) systems (with a few exceptions, e.g., the Virgo cluster, Urban et al. 2011). Cluster mass may therefore play a more important role in gas clumping than dynamical state.

4. An extended gas (>0.62 Mpc) is observed to the north of the A1750N subcluster along the large-scale structure, where one would expect to detect the densest part of the WHIM in a filament, near a massive cluster. The measured temperature (0.8–1 keV), density, and radial extent of this cool gas are consistent with the WHIM emission. The thermodynamical state of the gas at that radius (i.e., self-similar entropy profile, and gas mass fraction consistent with the cosmic value) favors the WHIM emission interpretation. However, a deeper observation with *Chandra* resolution is required to distinguish this diffuse filamentary gas from an infalling substructure, or gas from ram pressure-stripping.

REFERENCES

Ahn, C. P., Alexandroff, R., Allende Prieto, C., et al. 2014, ApJS, 211, 17
Akamatsu, H., Hoshino, A., Ishisaki, Y., et al. 2011, PASJ, 63, 1019
Anders, E., & Grevesse, N. 1989, GeCoA, 53, 197
Andrade-Santos, F., Jones, C., Forman, W. R., et al. 2015, ApJ, 803, 108
Arnaud, K. A. 1996, adass V, 101, 17
Arnaud, M., Pratt, G. W., Piffaretti, R., et al. 2010, A&A, 517, A92
Bautz, M. W., Miller, E. D., Sanders, J. S., et al. 2009, PASJ, 61, 1117
Beers, T. C., Flynn, K., & Gebhardt, K. 1990, AJ, 100, 32
Beers, T. C., Geller, M. J., & Huchra, J. P. 1982, ApJ, 257, 23
Belsole, E., Pratt, G. W., Sauvageot, J.-L., & Bourdin, H. 2004, A&A, 415, 821
Blanton, E. L., Sarazin, C. L., McNamara, B. R., & Wise, M. W. 2001, ApJL, 558, L15
Bonamente, M., Hasler, N., Bulbul, E., et al. 2012, NJPh, 14, 025010
Bulbul, G. E., Hasler, N., Bonamente, M., & Joy, M. 2010, ApJ, 720, 1038
Bulbul, G. E., Hasler, N., Bonamente, M., et al. 2011, A&A, 533, A6
Bulbul, G. E., Smith, R. K., Foster, A., et al. 2012, ApJ, 747, 32
Cavaliere, A., Lapi, A., & Fusco-Femiano, R. 2011, ApJ, 742, 19
De Grandi, S., & Molendi, S. 2002, ApJ, 567, 163
De Lucia, G., Poggianti, B. M., Aragón-Salamanca, A., et al. 2004, ApJL, 610, L77
Dolag, K., Meneghetti, M., Moscardini, L., Rasia, E., & Bonaldi, A. 2006, MNRAS, 370, 656
Donnelly, R. H., Forman, W., Jones, C., et al. 2001, ApJ, 562, 254
Eckert, D., Molendi, S., Owers, M., et al. 2014, A&A, 570, A119
Eckert, D., Molendi, S., Vazza, F., Ettori, S., & Paltani, S. 2013, A&A, 551, A22
Evrard, A. E., Bialek, J., Busha, M., et al. 2008, ApJ, 672, 122
Fabricant, D., Fata, R., Roll, J., et al. 2005, PASP, 117, 1411
Forman, W., Bechtold, J., Blair, W., et al. 1981, ApJL, 243, L133
Foster, A. R., Ji, L., Smith, R. K., & Brickhouse, N. S. 2012, ApJ, 756, 128

Fujita, Y., Ohira, Y., & Yamazaki, R. 2013, ApJL, 767, L4
Fusco-Femiano, R., & Lapi, A. 2014, ApJ, 783, 76
Gal, R. R., de Carvalho, R. R., Lopes, P. A. A., et al. 2003, AJ, 125, 2064
Gladders, M. D., & Yee, H. K. C. 2000, AJ, 120, 2148
Gladders, M. D., & Yee, H. K. C. 2005, ApJS, 157, 1
Hasler, N., Bulbul, E., Bonamente, M., et al. 2012, ApJ, 748, 113
Hickox, R. C., & Markevitch, M. 2006, ApJ, 645, 95
Hoshino, A., Henry, J. P., Sato, K., et al. 2010, PASJ, 62, 371
Huchra, J. P., Geller, M. J., & Corwin, H. G., Jr. 1995, ApJS, 99, 391
Humphrey, P. J., Buote, D. A., Brighenti, F., et al. 2012, ApJ, 748, 11
Ichikawa, K., Matsushita, K., Okabe, N., et al. 2013, ApJ, 766, 90
Ichinohe, Y., Werner, N., Simionescu, A., et al. 2015, MNRAS, 448, 2971
Ishisaki, Y., Maeda, Y., Fujimoto, R., et al. 2007, PASJ, 59, 113
Jones, D. H., Saunders, W., Read, M., & Colless, M. 2005, PASA, 22, 277
Kalberla, P. M. W., Burton, W. B., Hartmann, D., et al. 2005, A&A, 440, 775
Kawaharada, M., Okabe, N., Umetsu, K., et al. 2010, ApJ, 714, 423
Komatsu, E., Smith, K. M., Dunkley, J., et al. 2011, ApJS, 192, 18
Kriss, G. A., Cioffi, D. F., & Canizares, C. R. 1983, ApJ, 272, 439
Kuntz, K. D., & Snowden, S. L. 2000, ApJ, 543, 195
Landry, D., Bonamente, M., Giles, P., et al. 2013, MNRAS, 433, 2790
Lapi, A., Fusco-Femiano, R., & Cavaliere, A. 2010, A&A, 516, A34
Markevitch, M., & Vikhlinin, A. 2007, Phys. Rep., 443, 1
Miller, E. D., Bautz, M., George, J., et al. 2012, in AIP Conf. Ser. 1427, SUZAKU 2011: Exploring the X-ray Universe: Suzaku and Beyond (Melville, NY: AIP), 13
Molnar, S. M., Chiu, I.-N. T., Broadhurst, T., & Stadel, J. G. 2013, ApJ, 779, 63
Moretti, A., Campana, S., Lazzati, D., & Tagliaferri, G. 2003, ApJ, 588, 696
Nagai, D., Kravtsov, A. V., & Vikhlinin, A. 2007, ApJ, 668, 1
Nagai, D., & Lau, E. T. 2011, ApJL, 731, L10
Navarro, J. F., Frenk, C. S., & White, S. D. M. 1996, ApJ, 462, 563
Neumann, D. M. 2005, A&A, 439, 465
Paterno-Mahler, R., Randall, S. W., Bulbul, E., et al. 2014, ApJ, 791, 104
Planck Collaboration, Ade, P. A. R., Aghanim, N., et al. 2013a, A&A, 550, A131
Planck Collaboration, Ade, P. A. R., Aghanim, N., et al. 2013b, A&A, 550, A134
Pratt, G. W., Arnaud, M., Piffaretti, R., et al. 2010, A&A, 511, A85
Randall, S., Nulsen, P., Forman, W. R., et al. 2008, ApJ, 688, 208
Randall, S. W., Jones, C., Kraft, R., Forman, W. R., & O'Sullivan, E. 2009, ApJ, 696, 1431
Randall, S. W., Sarazin, C. L., & Ricker, P. M. 2002, ApJ, 577, 579
Reiprich, T. H., Basu, K., Ettori, S., et al. 2013, SSRv, 177, 195
Russell, H. R., Sanders, J. S., & Fabian, A. C. 2008, MNRAS, 390, 1207
Sato, K., Matsushita, K., Yamasaki, N. Y., Sasaki, S., & Ohashi, T. 2014, PASJ, 66, 85
Serlemitsos, P. J., Soong, Y., Chan, K.-W., et al. 2007, PASJ, 59, 9
Simionescu, A., Allen, S. W., Mantz, A., et al. 2011, Sci, 331, 1576
Simionescu, A., Werner, N., Urban, O., et al. 2013, ApJ, 775, 4
Simionescu, A., Werner, N., Urban, O., et al. 2015, ApJL, 811, L25
Smith, R. K., Brickhouse, N. S., Liedahl, D. A., & Raymond, J. C. 2001, ApJL, 556, L91
Su, Y., Buote, D., Gastaldello, F., & Brighenti, F. 2015, ApJ, 805, 104
Sun, M., Voit, G. M., Donahue, M., et al. 2009, ApJ, 693, 1142
Tawa, N., Hayashida, K., Nagai, M., et al. 2008, PASJ, 60, 11
Urban, O., Simionescu, A., Werner, N., et al. 2014, MNRAS, 437, 3939
Urban, O., Werner, N., Simionescu, A., Allen, S. W., & Bohringer, H. 2011, MNRAS, 414, 2101
Valentinuzzi, T., Poggianti, B. M., Fasano, G., et al. 2011, A&A, 536, AA34
Vazza, F., Eckert, D., Simionescu, A., Brüggen, M., & Ettori, S. 2013, MNRAS, 429, 799
Vikhlinin, A., Kravtsov, A. V., Burenin, R. A., et al. 2009, ApJ, 692, 1060
Voit, G. M., Kay, S. T., & Bryan, G. L. 2005, MNRAS, 364, 909
Walker, S. A., Fabian, A. C., & Sanders, J. S. 2013a, MNRAS, 435, 3221
Walker, S. A., Fabian, A. C., Sanders, J. S., & George, M. R. 2012a, MNRAS, 427, L45
Walker, S. A., Fabian, A. C., Sanders, J. S., & George, M. R. 2012b, MNRAS, 424, 1826
Walker, S. A., Fabian, A. C., Sanders, J. S., George, M. R., & Tawara, Y. 2012c, MNRAS, 422, 3503
Walker, S. A., Fabian, A. C., Sanders, J. S., Simionescu, A., & Tawara, Y. 2013b, MNRAS, 432, 554
Werner, N., Finoguenov, A., Kaastra, J. S., et al. 2008, A&A, 482, L29
Wik, D. R., Sarazin, C. L., Ricker, P. M., & Randall, S. W. 2008, ApJ, 680, 17